

Redox and phase behavior of Pd-substituted (La,Sr)CrO₃ perovskite solid oxide fuel cell anodes



Victor Y. Zenou^{a,b,1}, Daniel E. Fowler^{c,1}, Romain Gautier^c, Scott A. Barnett^a,
Kenneth R. Poeppelmeier^c, Laurence D. Marks^{a,*}

^a Department of Materials Science and Engineering, Northwestern University, Evanston, IL 60208, USA

^b Department of Materials, Nuclear Research Center, Negev, P.O. Box 9001, 84190 Beer-Sheva, Israel

^c Department of Chemistry, Northwestern University, Evanston, IL 60208, USA

ARTICLE INFO

Article history:

Received 10 June 2016

Received in revised form 5 August 2016

Accepted 5 September 2016

Available online xxxx

Keywords:

Solid oxide fuel cell

Perovskite

Transmission electron microscope (TEM),

scanning transmission electron microscope

(STEM), X-ray diffraction (XRD)

Electrochemical impedance spectroscopy (EIS)

ABSTRACT

The use of palladium and strontium in LaCrO₃ perovskites for solid oxide fuel cell anodes is known to lead to improved performance, in part due to the formation of palladium at the surface under reducing conditions that can act as a catalyst, with regeneration of the catalyst possible by cycling between oxidizing and reducing conditions. Whether this cycling involves dissolution and exsolution of the palladium into the perovskite is unclear. We describe a detailed analysis of the perovskites La_{0.8}Sr_{0.2}Cr_{1-x}Pd_xO_{3-δ} (LSCrPd, nominal stoichiometry $x = 0.1$ and 0.2) under reducing and oxidizing conditions. A LSCrPd perovskite was found to be the main phase, further confirmed by transmission electron microscopy. Secondary phases including metallic Pd, PdO, and La₄PdO₇, as well as SrCrO₄, were also present. Some phases, such as PdO, SrCrO₄, and La₄PdO₇, were no longer present following reduction while other phases such as metallic Pd and La₂O₃, were found in increasing amounts. When used as active solid oxide fuel cell anode layers both with and without Gd_{0.1}Ce_{0.9}O_{2-β} (GDC) in La_{0.9}Sr_{0.1}Ga_{0.8}Mg_{0.2}O_{3-ε}/La_{0.4}Ce_{0.6}O₂ electrolyte-supported cells, SOFCs with anodes containing GDC and higher amounts of Pd demonstrated higher maximum power densities and lower anode polarization resistances compared to cells with GDC-free, lower Pd content anodes. While the Pd is important to improve the anode performance, the results indicate that cycling does not lead to simple dissolution/exsolution into the perovskite, instead many other phases are present while a limited amount of Pd was actually observed in the perovskite.

© 2016 Elsevier B.V. All rights reserved.

1. Introduction

Solid oxide fuel cells (SOFCs) are appealing as energy conversion devices due to their low toxic emissions, high efficiency, and, especially, fuel flexibility [1,2]. Of the different materials available for use as SOFC anodes, nickel-yttria stabilized zirconia (Ni-YSZ) is the most widely used due to its excellent electronic conductivity, compatibility with other SOFC components, and catalytic activity for fuel oxidation [3,4]. Ni-YSZ anodes suffer from some significant drawbacks, however, including instability to redox cycling, coarsening of Ni, and sulfur poisoning and carbon coking during operation under hydrocarbon fuel sources [3,5–7].

Perovskites are one class of materials that are resistant to the drawbacks experienced by Ni-YSZ. Among the many perovskites that have been studied as alternatives to Ni-based anodes [8–12], LaCrO₃-based materials, belonging to the ABO₃ perovskite family, have shown particular promise owing to their mixed ionic/electronic conductivity and

good stability over a wide range of oxygen partial pressures [13,14]. This compound's simple perovskite crystal structure allows for relative ease of substitution at the A- and B-sites modifying the conductivity and stability properties. For instance, substituting Sr for La at the A-site in limited concentrations results in perovskites that are stable in both oxidizing and reducing conditions and that are ionically conductive due to increased oxygen vacancy content [15,16]. The presence of Cr at the B-site increases stability in reducing atmospheres but is unfortunately accompanied by a loss of conductivity, with LaCrO₃ being the least ionically conductive of all the transition metal lanthanum perovskite oxides [17,18]. To obtain the desired properties in LaCrO₃ compounds, it thus becomes necessary to balance these competing effects by substituting different metals at both the A- and B-sites. The B-site cation can be particularly important for increasing oxygen deficiency, which in turn increases the oxygen diffusivity that can improve the kinetics of electrochemical fuel oxidation [19–22]. Nonetheless, these perovskite anodes typically show relatively slow oxidation kinetics (high polarization resistance) compared to the Ni-based anodes, due to the lack of a catalyst for dissociating the H₂ fuel [23,24].

Various metals, including Mn, Fe, and Co, have been explored as B-site substituents for Cr in La_{1-x}Sr_xCrO₃ [25–27]. These metals were

* Corresponding author.

E-mail address: l-marks@northwestern.edu (L.D. Marks).

¹ Both authors contributed equally to this work.

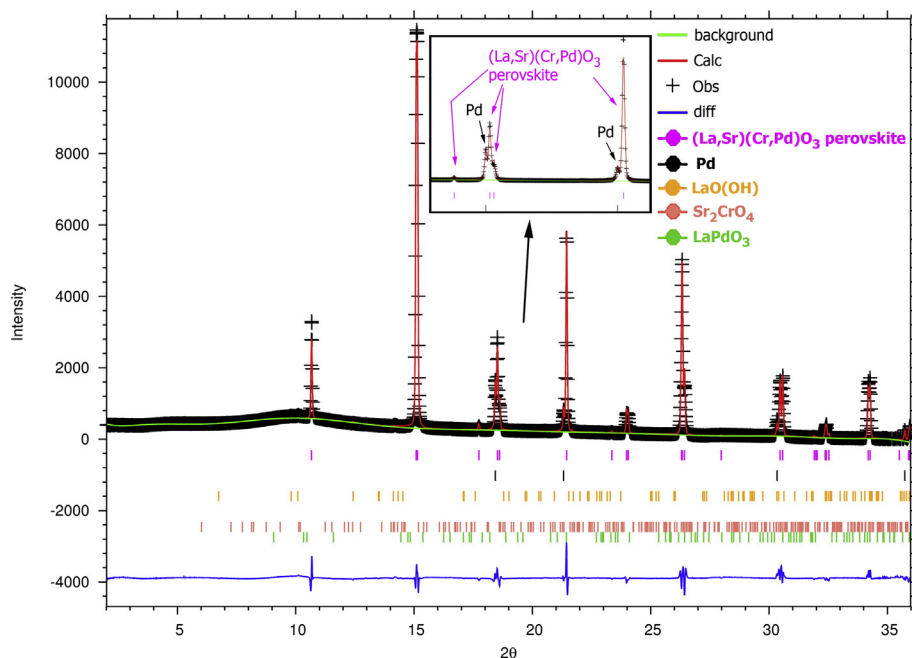


Fig. 1. Observed (black +), calculated (red line), background (green line), and difference (blue line) profile patterns of diffraction measurements on the LSCrPd10 powder taken during heating at 790 °C in 4% H₂/96% He. The positions of the reflections of all phases are shown as colored tick marks. The inset shows a close up view of several $R\bar{3}c$ perovskite reflections and one Pd reflection. The Profile and Bragg R values were $R_p = 4.1\%$, $R_{wp} = 7.7\%$ and $\chi^2 = 2.3$. (For interpretation of the references to color in this figure legend, the reader is referred to the web version of this article.)

found to largely improve the conductivity and catalytic activity toward hydrocarbons compared to the Cr-only perovskites. When catalytic metals such as Ru, Ni, and Pd were substituted in for Cr in $\text{La}_{1-x}\text{Sr}_x\text{CrO}_{3-\delta}$, the ensuing mixed perovskites demonstrated marked improvement in anode performance, obtaining low anode polarization resistance $R_{p,A}$ values [28–30]. The observed improvements were attributed in large part to the nucleation at the oxide surfaces of metal nanoparticles under reducing anode conditions [28,29,31]. The resultant particles presumably act as catalysts to promote the anode oxidation reaction and thus lower $R_{p,A}$.

One of these B-site substituents, the metal Pd, has demonstrated particular success at improving anode performance for the $\text{La}_{1-x}\text{Sr}_x\text{CrO}_{3-\delta}$ system. Originally studied as automotive emissions control catalysts [32–34], applications of Pd-substituted perovskite oxides expanded to include SOFC anodes. Their appeal as anodes derives from the ability of the Pd nanoparticles produced during exposure to reducing atmospheres to disappear upon re-exposure to oxidizing atmospheres, leaving only the bulk perovskite remaining. When applied as SOFC anodes, Pd-substituted perovskites have proved to be quite robust. For instance, the perovskite anodes $(\text{La,Sr})(\text{Cr,Pd})\text{O}_{3-\delta}$ and $(\text{La,Sr})(\text{Fe,Mn,Pd})\text{O}_{3-\delta}$ yielded lower $R_{p,A}$ values and higher maximum power densities compared to the Pd-free compounds $(\text{La,Sr})\text{CrO}_{3-\delta}$

and $(\text{La,Sr})(\text{Fe,Mn})\text{O}_{3-\delta}$ [30,35]. In a recent study on the improved anode performance of $(\text{La,Sr})\text{CrO}_{3-\delta}$ -based anodes upon the addition of Pd [30], it could not be confirmed whether Pd was substituting into the perovskite during either the initial synthesis or redox cycling. While Pd would be expected to occupy the B-site in $(\text{La,Sr})\text{CrO}_{3-\delta}$ since it is typically found with sixfold coordination in perovskites, all X-ray diffraction reflections of metallic Pd overlap with some of those from the $(\text{La,Sr})\text{CrO}_3$. Thus, it could not be determined whether Pd remained in excess or had fully substituted into the mixed perovskite solid solution. Although extended X-ray absorption fine structure (EXAFS) measurements confirmed a change in the oxidation state of Pd between 0 and +2 during redox cycling, they did not identify whether the change came from Pd redissolving into the perovskite or a different oxide phase [30]. Whether Pd dissolution into and exsolution out of the perovskite lattice actually occurs and plays a significant role in the regenerative performance of these materials when in SOFC anodes thus remains to be determined.

In this work, two different perovskites, synthesized as the nominal compositions $\text{La}_{0.8}\text{Sr}_{0.2}\text{Cr}_{1-x}\text{Pd}_x\text{O}_{3-\delta}$ (LSCrPd, $x = 0.1$ and 0.2) were assessed in detail structurally as potential regenerative SOFC anodes. The two oxide powders, synthesized here and hereafter denoted, e.g. LSCrPd10 for the $x = 0.1$ composition, were treated in conditions similar to those experienced at the anode, that is, heated to 800 °C and exposed alternately to hydrogen gas diluted in argon and oxygen, and were characterized both in situ and ex situ using high resolution powder X-ray diffraction and (scanning) transmission electron microscopy, respectively.

2. Experimental

2.1. Synthesis

Both perovskites $\text{La}_{0.8}\text{Sr}_{0.2}\text{Cr}_{1-x}\text{Pd}_x\text{O}_{3-\delta}$ ($x = 0.1, 0.2$; LSCrPd) were synthesized using the Pechini combustion method, which is known to promote reactant mixing and therefore improve the phase purity of oxide products [36,37]. Soluble metal nitrate salts of La ($\text{La}(\text{NO}_3)_3 \cdot 6\text{H}_2\text{O}$, 99.9%, Alfa Aesar), Sr ($\text{Sr}(\text{NO}_3)_2$, 99.97%, Alfa Aesar),

Table 1
Structural parameters of LSCrPd10 during heating in 4% H₂/96% He at 790 °C.

Phase	Space group	Lattice parameters (Å)	Estimated weight percent
$(\text{La,Sr})(\text{Cr,Pd})\text{O}_{3-\delta}$ Perovskite	$R\bar{3}c$ (#167)	$a = 5.5382(1)$, $c = 13.4941(3)$	91.4
Pd	$Fm\bar{3}m$ (#225)	$a = 3.9324(1)$	5.9
LaO(OH)	$P2_1/m$ (#11)	$a = 4.472(7)$, $b = 3.996(5)$, $c = 6.687(9)$	0.3
Sr_2CrO_4	$Pna2_1$ (#33)	$a = 13.96(2)$, $b = 5.89(1)$, $c = 10.18(2)$	2.1
LaPdO ₃	$Pnma$ (#62)	$a = 5.69(6)$, $b = 8.05(6)$, $c = 5.64(5)$	0.3

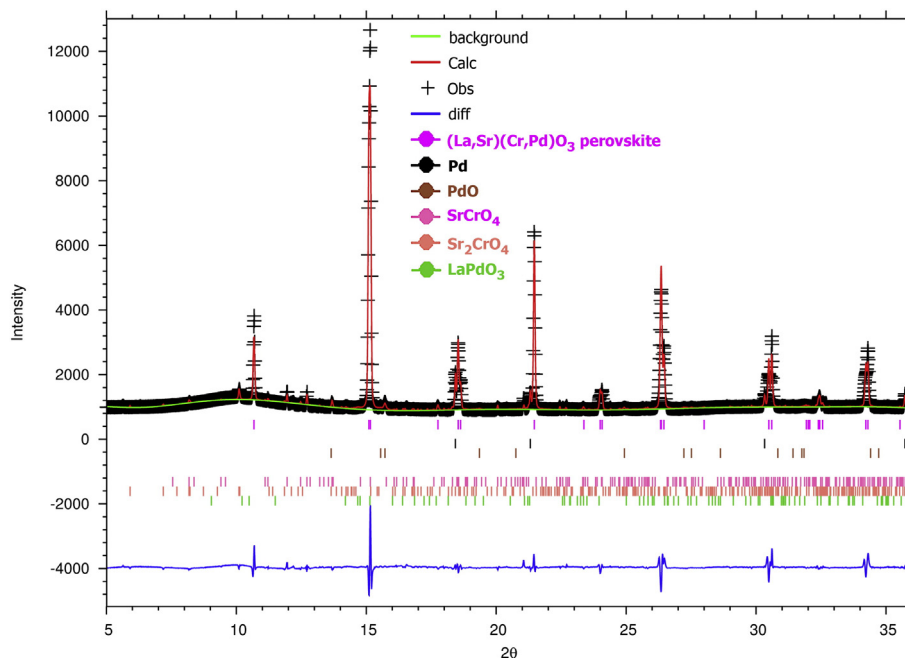


Fig. 2. Observed (black +), calculated (red line), background (green line), and difference (blue line) profile patterns of diffraction measurements on the LSCrPd10 powder after heating at 800 °C in O₂ for 1 h. Several phases in addition to the $R\bar{3}c$ perovskite that were observed and taken into account during refinement are also denoted by colored tick marks. $R_p = 2.2\%$, $R_{wp} = 4.1\%$ and $\chi^2 = 1.9$. (For interpretation of the references to color in this figure legend, the reader is referred to the web version of this article.)

Cr ($\text{Cr}(\text{NO}_3)_3 \cdot x\text{H}_2\text{O}$, 99.99%, Alfa Aesar) and Pd ($\text{Pd}(\text{NH}_3)_4(\text{NO}_3)_2$, 5.0 wt% Pd, Strem Chemicals) were dissolved in deionized water in a molar ratio of 8:2:9:1 or 8:2:8:2. Ethylenediaminetetraacetic acid (EDTA, 99 + %, Sigma Aldrich) was dissolved in concentrated NH_4OH in a molar ratio of 1:1 with the sum of all the moles of metal cations, and was then added to the aqueous nitrate solution. Citric acid (99.5 + %, Alfa Aesar) in a molar ratio of 2:1 with the sum of all the moles of metal cations was added to the combined solution, which was then heated to ~100 °C with stirring until a gel formed. The resultant gel was further heated at 250 °C for 3–6 h to produce a black resin. The resin was ground up to a fine powder and calcined at 800 °C for 3 h followed by heating to 1200 °C for 3 h.

The other oxides used for the SOFCs, including $\text{La}_{0.9}\text{Sr}_{0.1}\text{Ga}_{0.8}\text{Mg}_{0.2}\text{O}_{3-\epsilon}$ (LSGM) and $\text{La}_{0.4}\text{Ce}_{0.6}\text{O}_2$ (LDC), were synthesized using solid state reaction of stoichiometric amounts of La_2O_3 , SrCO_3 , Ga_2O_3 , MgO , and CeO_2 . The hygroscopic oxides La_2O_3 , Ga_2O_3 , and MgO were calcined at 900 °C for 1 h prior to weighing to drive off hydroxides and carbonates. The oxide powders were ball milled in ethanol for 24 h, filtered, and heated at 1000 °C for 4 h to form LSGM and at 1250 °C for 12 h to form LDC.

Table 2
Structural parameters of LSCrPd10 after heating in O₂ at 800 °C for 1 h.

Phase	Space group	Lattice parameters (Å)	Estimated weight percent
$(\text{La,Sr})(\text{Cr,Pd})\text{O}_3$ - _δ Perovskite	$R\bar{3}c$ (#167)	$a = 5.5336(1), c = 13.4798(4)$	85.2
Pd	$Fm\bar{3}m$ (#225)	$a = 3.9330(1)$	3.5
PdO	$P4_2/mmc$ (#131)	$a = 3.060(1), c = 5.372(5)$	1.6
SrCrO_4	$P2_1/n$ (#14)	$a = 7.180(1), b = 7.438(1), c = 6.881(1), \beta = 103.46(1)$	4.8
Sr_2CrO_4	$Pna2_1$ (#33)	$a = 14.083(8), b = 5.847(3), c = 10.189(4)$	3.8
LaPdO_3	$Pnma$ (#62)	$a = 6.00(4), b = 7.96(4), c = 5.66(3)$	1.1

2.2. In situ synchrotron X-ray powder diffraction

High-resolution synchrotron powder diffraction data were collected on LSCrPd compounds at beamline 17-BM at the Advanced Photon Source (APS), Argonne National Laboratory, at a wavelength of 0.7279 Å. Samples were loaded into 0.3 mm radius quartz capillary tubes open at both ends and capped with glass wool at both ends loosely enough to allow gas to flow. The capillary tubes containing the samples were secured in a compact reaction flow-cell and heated via two resistive furnace pieces also contained within the cell; a detailed description of the setup can be found elsewhere [38].

Diffraction data was collected using an amorphous silicon flat panel area detector from Perkin Elmer, in situ during heating from room temperature to 780–800 °C and cooling back and forth in various flowing gases, including O₂ (modeling synthetic oxidizing conditions), He (inert), and 4% H₂/96% He (modeling *in operando* SOFC anode conditions). Because diffraction experiments were designed to measure nearly instantaneous changes in reflections, full patterns were collected via quick scans lasting 10 s as well as longer scans lasting 60 s. The analysis software FIT2D was used to convert to one-dimensional diffraction data [39]. The patterns obtained fell within a 2θ range of 0–36°, with data points available every 0.018°. The data was analyzed using the Rietveld method with the GSAS code [40,41].

The as-synthesized samples, calcined at 1200 °C, were also measured using a Rigaku DMAX diffractometer (two-theta between 15° and 80°, at 0.05° steps) at room temperature, in order to analyze which phases exist in the samples before any redox treatment – see Supplemental Material.

2.3. (Scanning) transmission electron microscopy

TEM specimens were prepared by dispersing the powder in ethanol for 20–30 min. The suspension was left for 10–20 min before a drop was taken out from the upper part of the suspension and drop cast on a lacy carbon grid. The as synthesized and reduced powders were characterized by analytical scanning transmission electron microscope in a JEOL JEM2100 FaSTEM and a JEOL JEM-ARM200CF probe aberration

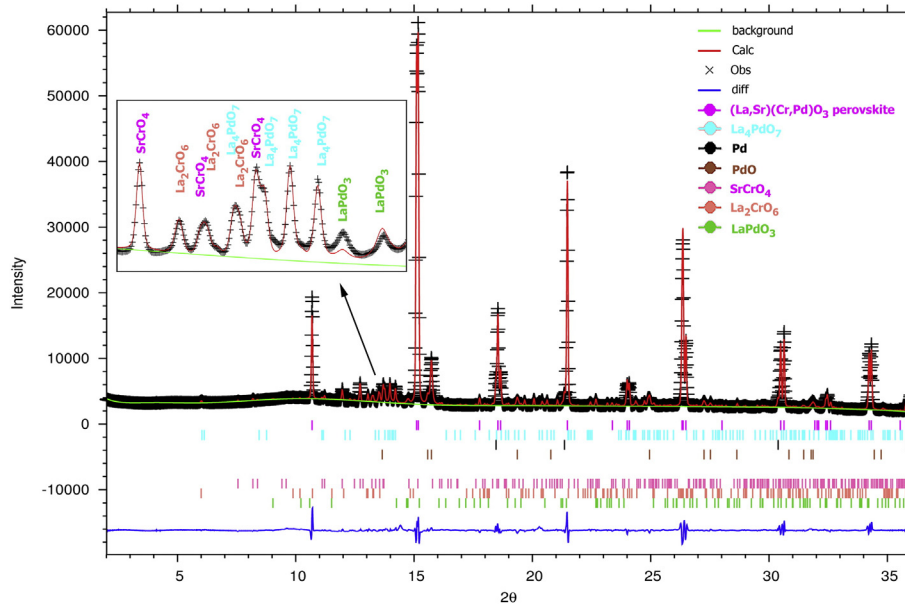


Fig. 3. Observed (black +), calculated (red line), background (green line), and difference (blue line) profile patterns of diffraction measurements on the LSCrPd20 powder after heating to 800 °C in O₂. Secondary phases in addition to the R $\bar{3}c$ perovskite that were observed and taken into account during refinement are also denoted as colored tick marks. The inset shows a close up view of several reflections from these side phases, including La₄PdO₇, LaPdO₃ and SrCrO₄. R_p = 2.5%, R_{wp} = 3.8% and χ^2 = 5.3. (For interpretation of the references to color in this figure legend, the reader is referred to the web version of this article.)

corrected 200 kV STEM/TEM. Compositional contrast images, enhancing the different phases, were acquired using high angle annular dark field (HAADF) imaging. Energy dispersive X-ray spectroscopy (EDS) was used to analyze the composition of the phases. Structural data was acquired via electron diffraction and high resolution in TEM mode. The data was analyzed and compared with the Java EMS software simulations code [42].

2.4. SOFC fabrication

SOFCs were assembled on LSGM electrolyte supports using techniques adapted from prior reports [19]. The active anode layers consisted of either single phase LSCrPd or LSCrPd composited with Gd_{0.1}Ce_{0.9}O_{2- β} (GDC, Nextech) in a 1:1 weight ratio. A La_{0.8}Sr_{0.2}CrO_{3- δ} (LSCr) current collector layer was applied on top of the anode active layer for both types of anodes. A thin layer of LDC was added between the anode and LSGM electrolyte to prevent reactions from occurring, as has been observed in prior reports on perovskite anodes on LSGM [43]. Cathode functional layers were composed of 1.) La_{0.6}Sr_{0.4}Co_{0.2}Fe_{0.8}O_{3- α} (LSCF,

Praxair) mixed with GDC in a 1:1 weight ratio and 2.) LSCF cathode current collector layers on top of the cathode composite.

LSGM was mixed with poly(vinyl butyral-co-vinyl alcohol-co-vinyl acetate) in ethanol as a slurry by ball milling for 24 h followed by uniaxial pressing of the powder into pellets 19 mm in diameter. Each pellet was bisque fired at 1200 °C for 4 h followed by deposition of a LDC ink onto one side via screen printing to serve as the barrier layer between the anode and electrolyte. These LDC-coated LSGM pellets were then heated at 1450 °C for 6 h to yield fully dense ceramic oxide supports measuring ~400 μ m in thickness.

Viscous inks of the electrode powders were prepared by ball milling the powders in ethanol for 24 h, drying, and mixing with an organic polymeric vehicle (Heraeus V737) on a three roll mill. The anode functional layer inks were applied onto the LDC sides of the dense LSGM supports using screen printing. Following deposition of the LSCr anode current collector inks directly on top of the functional layers, the support and anode—including active and current collector layers—were cofired at 1200 °C for 3 h. The anodes were circular with an area of 0.5 cm² and a thickness of ~30–40 μ m. For cathodes, the active LSCF-GDC layer was applied to the LSGM support using screen printing, after which the LSCF current collector was deposited directly on top. Both cathode layers were cofired simultaneously at 1000 °C for 3 h, resulting in circular cathodes 0.5 cm² in area and ~20–30 μ m thick. A gold paste (Heraeus, Inc.) was then applied on top of both electrodes' current collectors as a grid to serve as a contact to silver wires used for electrochemical testing.

2.5. Electrochemical testing

Full cell testing was performed using a previously described setup [19,44]. SOFCs were attached to alumina support tubes using a conductive silver paste (DAD-87, Shanghai Research Institute of Synthetic Resins) with anodes facing into the tube. The silver functioned to provide both a gastight seal and an electrical connection to gold anode current collector grids. A second alumina tube smaller in diameter was threaded through the main support tube and delivered humidified hydrogen (97% H₂/3% H₂O) to the anode at a flow rate of 50 sccm. Oxygen from the air served as an oxidant via exposure of the cathode to the ambient atmosphere. SOFCs were operated at 800 °C for periods up to 24 h.

Table 3

Structural parameters of LSCrPd20 during heating in O₂ at 800 °C.

Phase	Space group	Lattice parameters (Å)	Estimated weight percent
(La,Sr)(Cr,Pd)O ₃ - ₆ Perovskite	R $\bar{3}c$ (#167)	a = 5.5349(1), c = 13.4658(2)	70.9
La ₄ PdO ₇	C2/m (#12)	a = 13.599(1), b = 4.0651(4), c = 9.5194(9), β = 133.476(5)	4.9
Pd	Fm $\bar{3}m$ (#225)	a = 3.9280(1)	1.5
PdO	P4 ₂ /mmc (#131)	a = 3.0592(2), c = 5.3686(7)	9.1
SrCrO ₄	P2 ₁ /n (#14)	a = 7.1768(8), b = 7.4425(7), c = 6.8828(7), β = 103.49(1)	9.2
La ₂ CrO ₆	C2/c (#15)	a = 14.547(3), b = 4.431(1), c = 8.582(2), β = 107.29(2)	2.2
LaPdO ₃	Pnma (#62)	a = 5.797(3), b = 7.798(5), c = 5.871(5)	2.2

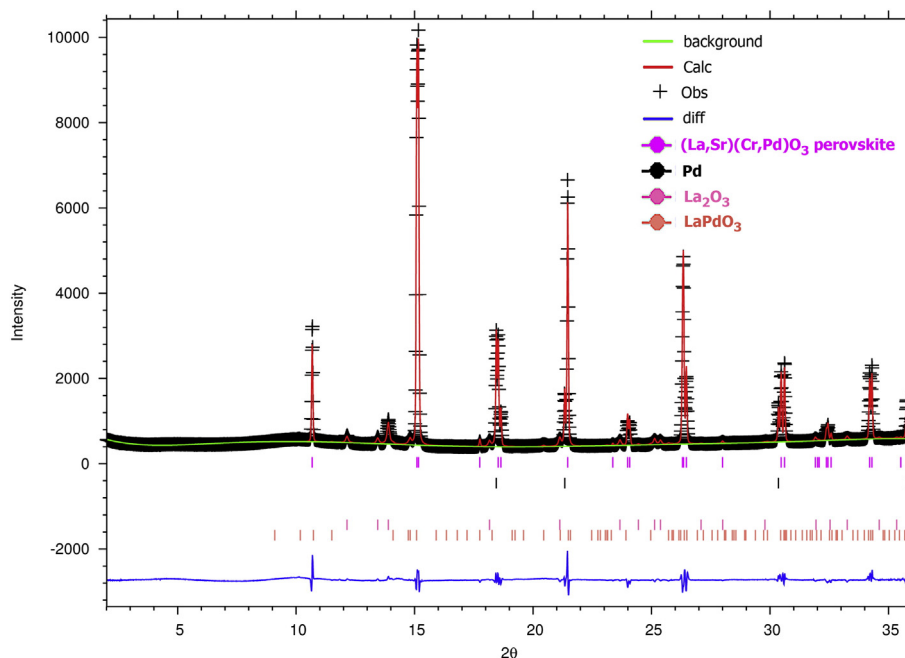


Fig. 4. Observed (black +), calculated (red line), background (green line), and difference (blue line) profile patterns of diffraction measurements on the LSCrPd20 powder taken after heating at 800 °C 4% H₂/96% He for 30 min. Additional phases besides the majority $R\bar{3}c$ perovskite phase that were observed and taken into account while refining are shown as colored tick marks, as well. $R_p = 2.3\%$, $R_{wp} = 3.6\%$ and $\chi^2 = 0.8$. (For interpretation of the references to color in this figure legend, the reader is referred to the web version of this article.)

Current–voltage and electrochemical impedance spectroscopy (EIS) were recorded using a four-probe single cell test setup (BAS-Zahner, IM-6). Impedance spectra were recorded at frequencies ranging from 0.1 Hz to 1 MHz with a 20 mV potential amplitude. EIS data fitting to an equivalent circuit was performed using the ZView software (Scribner).

3. Results

3.1. Structural characterization

The synthesized perovskites $\text{La}_{0.8}\text{Sr}_{0.2}\text{Cr}_{1-x}\text{Pd}_x\text{O}_{3-\delta}$ ($x = 0.1, 0.2$; in short LSCrPd10 and LSCrPd20, respectively) were heated to 800 °C under flowing gases which included O₂, He, and 4% H₂/96% He and were characterized during heating and gas exposure using in situ high resolution powder diffraction. For LSCrPd10, the sample was heated up to ~800 °C in 4% H₂/96% He, held in inert He at 800 °C for 20 min, and later held under O₂ at 800 °C for 1 h. Fig. 1 shows the diffraction pattern for LSCrPd10 after initially heating at 790 °C in 4% H₂/96% He, as well as the Rietveld profile analysis, fitting the pattern primarily to the rhombohedral $(\text{La,Sr})(\text{Cr,Pd})\text{O}_{3-\delta}$ perovskite in the $R\bar{3}c$ space group. At the final stages of the profile fitting, the La/Sr, Cr/Pd ratios (assuming La + Sr = 1 and Cr + Pd = 1) and oxygen nonstoichiometry δ were refined and stabilized at $x = -0.16$, $y = -0.002$ and $\delta = -0.06$, indicating

Table 4
Phases found by Rietveld analysis of synchrotron data of powder heated in H₂ at 800 °C.

Phase	Space group	Lattice parameters (Å)	Estimated weight percent
$(\text{La,Sr})(\text{Cr,Pd})\text{O}_{3-\delta}$ Perovskite	$R\bar{3}c$ (#167)	$a = 5.5382(1), c = 13.4752(2)$	83.4
Pd	$Fm\bar{3}m$ (#225)	$a = 3.9303(1)$	9.7
La ₂ O ₃	$P\bar{3}m1$ (#164)	$a = 3.968(1), c = 6.215(1)$	4.3
LaPdO ₃	$Pnma$ (#62)	$a = 5.92(1), b = 7.70(1), c = 5.82(1)$	2.6

as expected that these perovskites are indeed oxygen deficient ($x = \text{Sr/La}$; $y = \text{Pd/Cr}$). The results are shown in Table 8. The results of the profile fit also indicate at least four additional phases present in addition to the $R\bar{3}c$ perovskite phase (~91%); the estimated weight percent for each phase is shown in Table 1.

The rhombohedral $R\bar{3}c$ $(\text{La,Sr})(\text{Cr,Pd})\text{O}_{3-\delta}$ perovskite structure is expected, since LaCrO₃ undergoes a phase transformation from an orthorhombic $Pnma$ phase to a rhombohedral $R\bar{3}c$ phase above 280 °C or upon sufficient Sr substitution onto the A-site ($x > 0.15$ for $\text{La}_{(1-x)}\text{Sr}_x\text{CrO}_3$) [13,45]. Small amounts of metallic Pd (highlighted in the inset in Fig. 1), Sr₂CrO₄, LaPdO₃, and LaO(OH) totaling about 8.6 wt% were also found in the LSCrPd phase mixture. Metallic Pd composed the vast majority of the make-up of these secondary phases, about 5.9 of the 8.6 wt% total for the secondary phases. Having a majority of the secondary Pd source contained as Pd metal following reduction, as seen here, is consistent with prior reports on Pd-substituted perovskites [30,35]. Much smaller amounts of the remaining phases, Sr₂CrO₄, LaPdO₃, and LaO(OH), were identified in the mixture. Only the strongest reflections were observed for each of these minority phases, which were too weak for a full refinement to be performed on them.

Powder diffraction was also used to examine the LSCrPd10 phase mixture following heating at to 800 °C in O₂ for 1 h, after the initial reduction described above (Fig. 1). The diffraction pattern following this heating stage is shown in Fig. 2, along with the profile analysis. Similar to before, the oxygen nonstoichiometry δ was again refined during the final stages of refinement, stabilizing at ~0.002, indicating that following exposure to reducing conditions, the perovskite almost retains no oxygen deficiency for some time (at least 1 h) at high temperatures, in oxidizing conditions, similar to Khattak [13] results *et al.* on mixed $(\text{La,Sr})\text{CrO}_{3-\delta}$ perovskites. The results of the profile fit also indicate at least five additional phases present in addition to the $R\bar{3}c$ perovskite phase; the estimated weight percent for each phase is shown in Table 2.

The main phase identified in the mixture was again the $R\bar{3}c$ $(\text{La,Sr})(\text{Cr,Pd})\text{O}_{3-\delta}$ perovskite, with a weight percent of 85.2%, lower than the reduced LSCrPd10 sample discussed above. This decrease in the overall amount of perovskite upon re-oxidation is likely due to decomposition to the monoclinic secondary phase SrCrO₄, which has

Table 5

Average perovskite composition determined by EDS analysis for different LSCrPd samples as-synthesized or heated in air, and after exposure to 10% H₂ at 800 °C for 6 h.

Elemental energy line	Measured LSCrPd10 composition (standard deviation)		Measured LSCrPd20 composition (standard deviation)	
	Heated in O ₂	Heated in H ₂	As-synthesized (heated in O ₂)	Heated in H ₂
La L-edge	52.1 (1.8)	49.3 (3.3)	52.6 (2.7)	51.2 (2.0)
Sr K-edge	2.0 (0.8)	4.0 (2.4)	1.6 (1.4)	1.9 (0.9)
Cr K-edge	44.9 (1.3)	46.3 (2.4)	44.2 (2.1)	45.6 (2.3)
Pd L-edge	0.9 (0.9)	0.5 (0.5)	1.7 (1.4)	1.2 (0.7)

been shown to form in oxidizing conditions during B-site substitution into La_{1-x}Sr_xCrO₃ perovskites ($x > 0.1$), especially when metal nitrates are used as precursors, as in this study [15,46,47]. With less perovskite thus available for the Pd to dissolve into upon re-oxidation, the remaining metal either oxidizes to form PdO or remains as metallic Pd, both of which were observed in a previous study of oxidized samples of the LSCrPd20 perovskite [30]. These small amounts of SrCrO₄, PdO, and metallic Pd found in the LSCrPd phase mixture totaled about 10 wt%. The main perovskite phase's lattice parameters decreased compared to the reduced sample, with a 0.28% smaller cell volume, likely owing to an

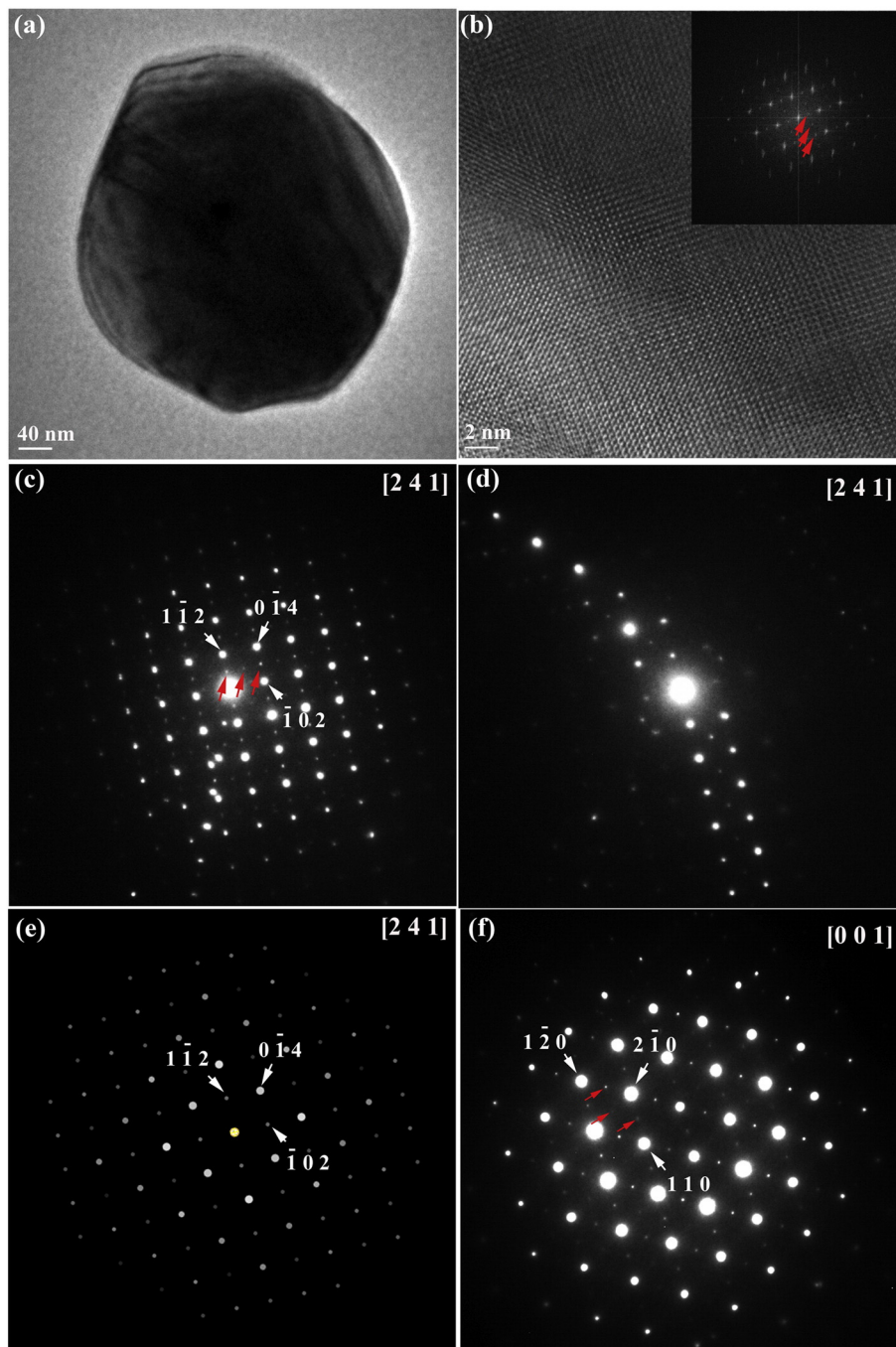


Fig. 5. TEM images of the as-synthesized LSCrPd10 perovskite showing the general particle morphology (a); high resolution (HR) imaging (zone axis = [241]) with the corresponding fast Fourier transform (FFT) presented as an inset (b); selected area electron diffractions (SAED) recorded along the [241] zone axis (c) and off that zone axis (d); SAED simulation conducted using the Java EMS software for [241] zone axis (e), and SAED along [001] zone axis (f). Extra experimental reflections can be seen highlighted by red arrows in (b), (c) and (f). (For interpretation of the references to color in this figure legend, the reader is referred to the web version of this article.)

increase in the amount of Pd substituted into the perovskite in the oxidizing conditions. For the secondary phases in all XRD experiments, lattice parameters were ~1% higher than room temperature values previously reported at room temperature, most likely due to thermal expansion [48–50]. When compared with reported values at higher temperatures, the observed lattice parameters for compounds such as SrCrO₄ displayed much better matches in lattice constants [51]. Additionally, a few small reflections of Sr₂CrO₄ and LaPdO₃ were also noted in the pattern. These phases were present in such small quantities (<5 wt%), however, that a full refinement could not be performed on them. For the perovskite LaPdO₃, only the strongest reflection (121) was observed at 14.8°, indicating this phase was present in very small quantities.

The LSCrPd20 specimen was similarly heated to 800 °C in flowing gases and characterized in situ using high resolution powder diffraction. As opposed to LSCrPd10, which was heated up to ~800 °C in dilute H₂ followed by exposure to O₂, LSCrPd20 was first heated up to 800 °C in O₂, held under inert He at 800 °C for 20 min, and finally held under 4% H₂/96% He for 30 min. Fig. 3 shows the diffraction pattern for LSCrPd20 after heating to 800 °C in O₂, with a Rietveld profile fit principally to the *R* $\bar{3}c$ space group. Once again at the final stage of the refinement process δ was refined to ~0.03.

The *R* $\bar{3}c$ (La,Sr)(Cr,Pd)O_{3- δ} perovskite was again the main component of the phase mixture, though with a weight percent of 70.9% as indicated in Table 3, it is the smallest fraction of perovskite of all the different phase analyses. This is likely from a combination of the fact that LSCrPd20 specimen is known to have an excess of palladium beyond the solubility limit in the perovskite and also since this measurement was taken in conditions most similar to the as-synthesized powder, which is well-known to form phases that decompose upon

reduction [30]. Minority amounts of the secondary phases metallic Pd, PdO, La₄PdO₇, SrCrO₄, La₂CrO₆ and LaPdO₃ were also identified and constituted ~29 wt% of the phase mixture. Of this 29%, almost 18% were phases containing Pd (metallic Pd, PdO, La₄PdO₇, and LaPdO₃), another strong indicator that a molar ratio of $x = 0.2$ in La_{0.8}Sr_{0.2}Cr_{1-x}Pd_xO_{3- δ} is well beyond the solubility limit of Pd in the La_{0.8}Sr_{0.2}CrO_{3- δ} perovskite.

After heating the LSCrPd20 phase mixture in 4% H₂/96% He at 800 °C for 30 min, powder diffraction was used to determine how the structure and phase make-up changed in reducing conditions. Fig. 4 shows the diffraction pattern following heating in reducing conditions as well as the profile analysis fit to the *R* $\bar{3}c$ space group used previously. Oxygen nonstoichiometry δ was again evaluated through refinement and found to be almost 0.21. Taking experimental uncertainty into consideration, this δ value was the highest calculated of all measurements, along with the LSCrPd10 measurement heated to 790 °C in 4% H₂/96% He, unsurprising considering that both of these diffraction measurements were taken in reducing conditions that were the most likely to lead to oxygen loss. Higher oxygen non-stoichiometry δ is typically observed for B-site substituted LaCrO₃ perovskites with less Cr on the B-site [19, 52], as was observed in our LSCrPd10 and LSCrPd20 perovskites. In addition to the majority *R* $\bar{3}c$ phase, secondary phases such as metallic Pd, La₂O₃, and LaPdO₃ were also identified in the pattern and are listed in Table 4 along with each phase's estimated weight percent.

The rhombohedral *R* $\bar{3}c$ (La,Sr)(Cr,Pd)O_{3- δ} perovskite continued to be the main phase in the mixture at a weight percent of 83.4%. As in the LSCrPd10 sample, the weight percent of this reduced LSCrPd20 was higher than that was found for the oxidized LSCrPd20 described above (70.7% above for oxidized versus 83.4% for reduced), likely because of the perovskite's higher stability in reducing conditions than the

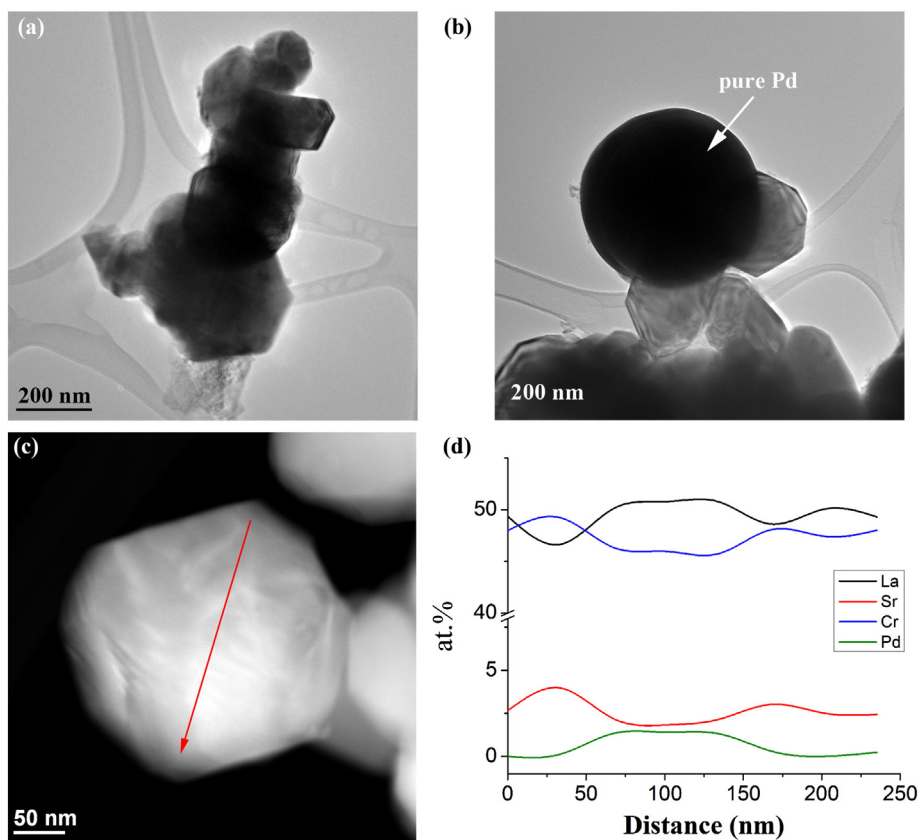


Fig. 6. Ex situ TEM/STEM imaging analysis of the LSCrPd10 specimen after heating at 800 °C for 6 h in ~10% H₂/3% H₂O in Ar showing: bright field imaging of (a) perovskite particles and (b) a relatively large particle (ca. 400 nm in diameter) consisting purely of metallic Pd; (c) high angle annular dark field (HAADF) imaging of another typical perovskite particle; and (d) results from an EDS line scan along the red line from (c). (For interpretation of the references to color in this figure legend, the reader is referred to the web version of this article.)

numerous side phases, such as La_4PdO_7 and SrCrO_4 , found in the measurements taken in oxidizing conditions. As with LSCrPd10, the calculated lattice parameters for the oxidized measurement increased slightly compared to the reduced measurement, with a 0.19% larger cell volume again attributed to less Pd substituting into the perovskite. The minority phases identified totaled 16.6 wt%, 14 wt% of which was metallic Pd (9.7%) and La_2O_3 (4.3%). Again the perovskite LaPdO_3 was identified from weak reflections and was determined to be present in only a small amount (2.6 wt%).

For the LSCrPd20 diffraction measurement in dilute H_2 , both metallic Pd and La_2O_3 increased in amount compared to the measurement taking place in O_2 , accounted for by the fact that several of the side phases that were stable in O_2 (PdO , SrCrO_4 , La_4PdO_7 , La_2CrO_6) are unstable in reducing conditions and decompose to lower oxidation state phases. Indeed, La_4PdO_7 is known to decompose to La_2O_3 and metallic Pd in reducing conditions at high temperatures [53,54], and La_2CrO_6 becomes La_2O_3 and LaCrO_3 under reducing conditions above 370 °C [46], accounting for the increase in the weight percent of these decomposition products. Additionally, upon decomposition in reducing conditions, the oxidized Pd-containing phases such as La_4PdO_7 and PdO likely do not reform, as neither of these were identified in the LSCrPd10 mixture after exposure first to H_2 then O_2 at ~ 800 °C. Thus, any recovery in

SOFC anode performance for these perovskites upon redox cycling, as had been observed in these and similar materials previously, [30,35] cannot be from these decomposed secondary phases and may instead be attributed to the catalytic metallic Pd exsolving out and redissolving into of the perovskite lattice.

3.2. (Scanning) transmission electron microscopy

To further determine the composition and behavior of the LSCrPd phase mixture in conditions similar to SOFC anodes, the LSCrPd powders were heated at 800 °C for 6 h in $\sim 10\%$ $\text{H}_2/3\%$ H_2O diluted in Ar and investigated ex situ using transmission electron microscopy (TEM) and energy dispersive X-ray spectroscopy (EDS) analysis, along with as-synthesized/ heated in air samples. Table 5 shows the average results of the EDS analysis performed on the as-synthesized and 10% H_2 reduced powders. While numerous particles were sampled via EDS during analysis of each powder, the estimated relative error of phase composition determined by EDS analysis through TEM was about 2–5% due to a number of different factors, including high background noise and overlapping peaks. Results of the analysis still indicate less Sr and Pd substituted into the $(\text{La,Sr})(\text{Cr,Pd})\text{O}_{3-\delta}$ than the nominal stoichiometry implies. Assuming a total sum of 100 at.% for all metal

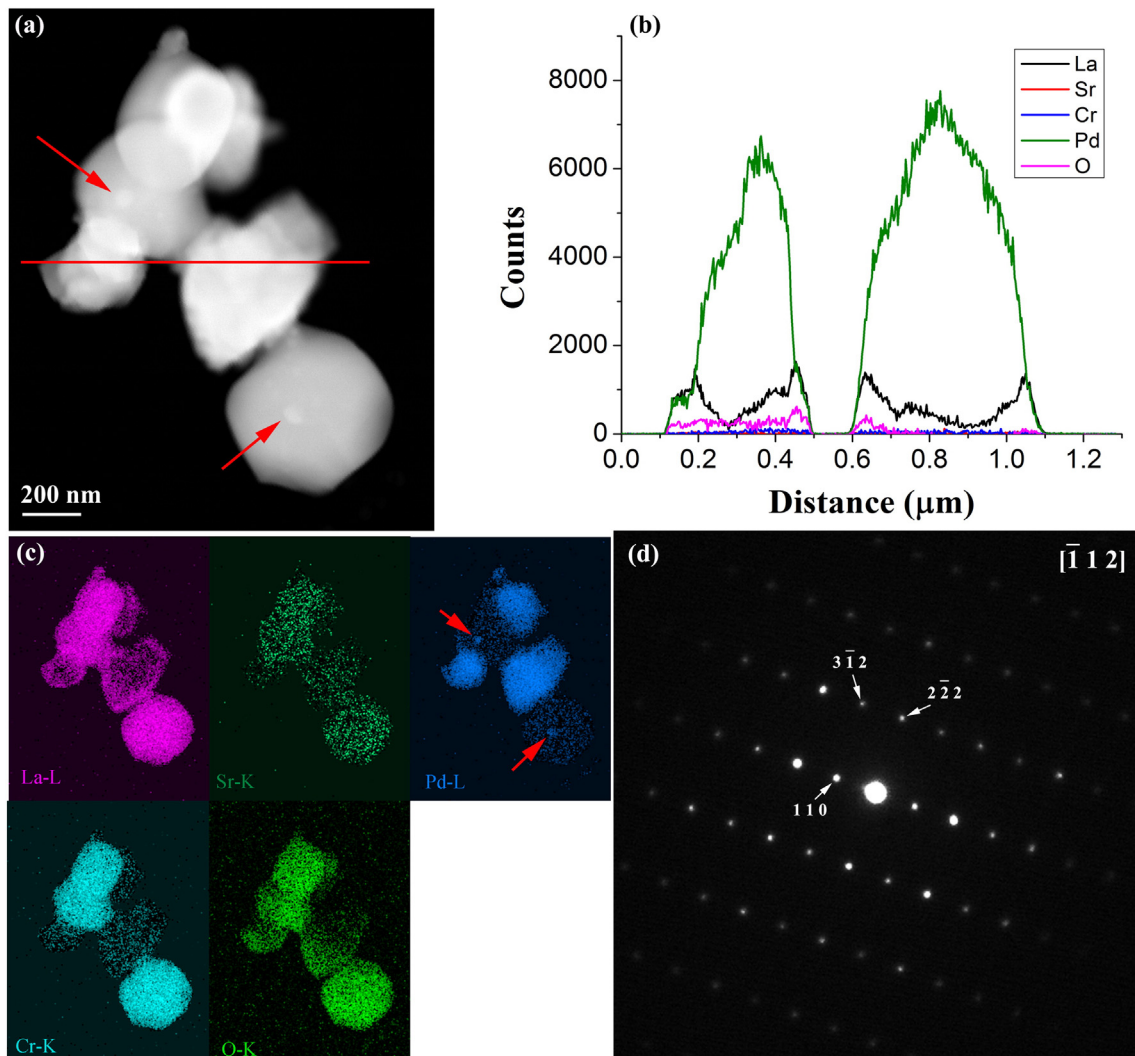


Fig. 7. STEM images of the as-synthesized LSCrPd20 perovskite showing: (a) HAADF imaging of the general particle morphology; (b) results from an EDS line scan along the red line in “a”; (c) results from EDS elemental mapping of La, Sr, Cr, Pd, and O on the particles shown in “a”; and (d) SAED recorded along the $[\bar{1} 1 2]$ zone axis of La_7Pd_3 , a Pd-core/Pd-La-shell-structured secondary phase. Red arrows highlight small particles which are probably metallic Pd. (For interpretation of the references to color in this figure legend, the reader is referred to the web version of this article.)

substituents, maximum atomic percentages of only 4.0 and 1.9 were found for Sr in LSCrPd10 and LSCrPd20, respectively, and maximum atomic percentages of only 0.9 and 1.7 were found for Pd in LSCrPd10 and LSCrPd20, respectively. Prior work has experimentally observed the solubility of Sr in $\text{La}_{1-x}\text{Sr}_x\text{CrO}_3$ to be at $x = 0.10 \pm 0.02$ at 950°C [15]. Higher Cr content perovskites such as $\text{La}_{1-x}\text{Sr}_x\text{CrO}_3$ would be present if Pd is not able to successfully substitute into them, which would lead to a lower Sr solubility, as observed here. The large number of Sr- and Pd-containing secondary phases observed via diffraction, discussed above, and via a parallel TEM/STEM study, discussed later, confirms that the Sr and Pd content in the perovskites are lower than the nominal stoichiometries of $\text{La}_{0.8}\text{Sr}_{0.2}\text{Cr}_{0.8}\text{Pd}_{0.2}\text{O}_{3-\delta}$ and $\text{La}_{0.8}\text{Sr}_{0.2}\text{Cr}_{0.9}\text{Pd}_{0.1}\text{O}_{3-\delta}$.

Fig. 5 shows TEM images used for phase analysis of the as-synthesized LSCrPd10 mixture, including particle morphology (a), high resolution (HRTEM) imaging (b), selected area electron diffraction (SAED) along [241] on (c) and off zone axis (d) with Java EMS software diffraction simulation (e), and SAED along [001] acquired for the same powders sintered at 1200°C for 3 h (f). The majority of the particles observed via TEM were identified as the (La,Sr)(Cr,Pd)O₃ perovskite, corroborating the powder diffraction data which consistently identifying the perovskite as the majority phase. Depending on the direction of view, these particles typically had either a hexagonal or partially faceted morphology. Several of these particles analyzed by EDS (Table 5) were found to have an average composition of 52.1 at.% La, 2.0 at.% Sr, 44.9 at.% Cr, and 0.9 at.% Pd, showing lower amounts of Sr and Pd compared to the nominal stoichiometry, as seen in EDS on all the perovskite samples. Upon closer examination of the perovskite structure using HRTEM imaging and SAED, a few extra reflections were identified, denoted with red arrows in the fast Fourier

transform (FFT) of the HRTEM image in the inset of Fig. 5b and in the SAED image in Fig. 5c. When the TEM specimen was tilted off-zone axis, the reflections located in the center were the only extra reflections remaining in view (Fig. 5d). Therefore some of these reflections could occur due to dynamical scattering probably a result of some type of ordering via a group-subgroup relation, as all these extra reflections could be easily index using new lattice parameters $a' = 2a$ and $c' = c$ (“a” and “c” are the original parameters of the perovskite). This ordering is likely affected by temperature, as well, as no extra reflections at the same positions were observed in the in situ high temperature diffraction data on the LSCrPd10 perovskite.

As seen in the powder diffraction data in O₂ at 800°C presented above, multiple non-perovskite Pd-rich phases could be observed. Particles of one such phase with an average composition of 17 at.% La, 5 at.% Cr, and 78 at.% Pd were observed via TEM imaging and EDS analysis. SAED analysis of these particles suggests they have the structure of the metallic compound La_7Pd_3 , a phase which was not observed by in situ diffraction of LSCrPd10 at 800°C in O₂. The observation of this phase only at room temperature via TEM and SAED could be because either it being present only in very small amounts undetectable by powder diffraction or from its instability in the high temperature, oxidizing conditions under which in situ powder diffraction measurements were recorded.

The same LSCrPd10 specimen characterized by TEM imaging in Fig. 5 was heated at 800°C for 6 h in $\sim 10\% \text{H}_2/3\% \text{H}_2\text{O}$ in Ar and further examined ex situ using TEM. Fig. 6 shows TEM characterization of the reduced LSCrPd10 perovskite, including (a) bright field image of some perovskite particles, (b) particles high in metallic Pd content that were also identified during imaging, (c) high angle annular dark field (HAADF) image displaying a perovskite particle, and (d) results from the EDS

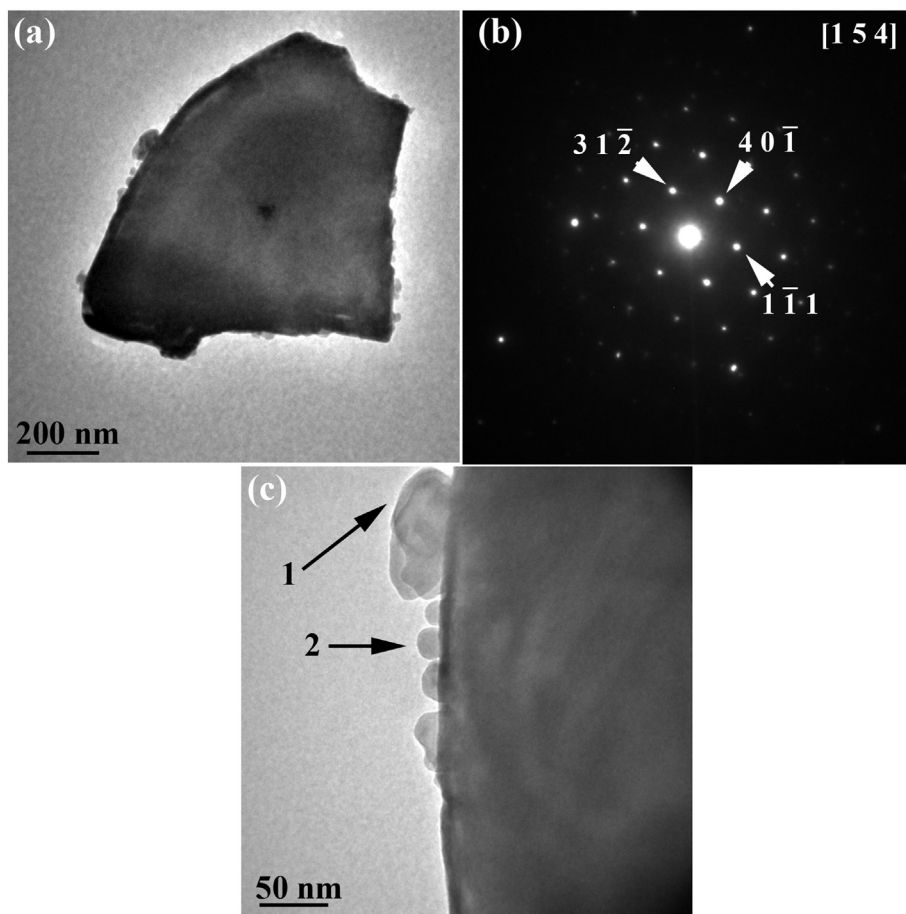


Fig. 8. TEM images of oxide phases observed in the as-synthesized LSCrPd20 mixture, including (a) bright field imaging and (b) SAED of La_4PdO_7 along the [154] zone axis as well as (c) higher magnification showing smaller Sr- and Cr-containing oxide particles, denoted as “1” and “2” by arrows in the image, on the surface of the La_4PdO_7 phase.

line scan on the particle from (c). The main phase observed was again the $(\text{La,Sr})(\text{Cr,Pd})\text{O}_3$ perovskite, confirmation that the perovskite does not totally decompose and remains stable in reducing conditions. Numerous perovskite particles, such as those shown in Fig. 6a and c, were analyzed by EDS and found to have an average composition of 49.3 at.% La, 4.0 at.% Sr, 46.3 at.% Cr, and 0.5 at.% Pd, also listed in Table 5. Reduction thus decreased the amount of Pd substituted into the perovskite from 0.9 at.% in the as-synthesized LSCrPd10 sample discussed above, as originally proposed in prior works with the LSCrPd perovskites [30]. While numerous small and relatively large particles (ca. 400 nm in diameter Fig. 6b) high in Pd content were identified adjacent to the perovskite particles throughout the TEM specimen, EDS analysis of the perovskite particle along the red line shown in Fig. 6c analysis showed that the concentration of Pd goes from zero at the particle edges to a maximum of 1.4 at.% in the center (Fig. 6d). The perovskite thus does still retain some Pd within the structure, though it appears to be concentrated more highly in the center of particles along with La, while Sr and Cr appear to be more highly concentrated at the particle edges.

Fig. 7 shows electron imaging analysis performed on the as-synthesized LSCrPd20 mixture, including (a) typical particle morphology displayed via HAADF; results (b) from an EDS line scan along the red line across a particle in (a) and (c) from EDS elemental mapping of La, Sr, Cr, Pd, and O on the particle shown in (a); (d) SAED recorded along the $[\bar{1}12]$ zone axis of La_7Pd_3 , a Pd-core/Pd-La-shell-structured secondary phase. Most of the particles identified were again the $(\text{La,Sr})(\text{Cr,Pd})\text{O}_3$ perovskite, with an average composition of 52.6 at.% La, 1.6 at.% Sr, 44.2 at.% Cr, and 1.7 at.% Pd, also listed in Table 5. The Pd content in the observed

LSCrPd20 perovskite particles was calculated to be about 2 times higher than that calculated for the LSCrPd10 perovskite particles presented above, consistent with the ratio of Pd content between the nominal stoichiometry of LSCrPd20 and LSCrPd10. Despite this, however, much lower amounts of Sr and Pd were observed compared to the nominal stoichiometry, likely a result of the formation of the numerous side phases observed by both powder diffraction, discussed above, and TEM, discussed here. This excess of Pd, which could not be detected as substituted into the perovskites, was instead observed partly as small metallic Pd nanoparticles on the perovskite surfaces and can be seen highlighted with red arrows as small white spots in Fig. 7a and as small light blue spots in Fig. 7c. Additionally, particles that appeared as metallic LaPd phases with La:Pd ratios ranging from 1:1 to 1:4 or 1:8 were frequently observed. These LaPd particles were often observed alongside the LSCrPd20 perovskite particles and sometimes displayed core-shell type structures with Pd-rich and La-Pd-rich shells, as shown by the EDS line scan results in Fig. 7b from the particles in Fig. 7a. The LaPd particles were further examined using SAED, the results from which are shown in Fig. 7d and indicated a structural fit to the compound La_7Pd_3 . The average composition of these LaPd particles as calculated by EDS was 43.4 at.% La, 1.1 at.% Cr, and 55.5 at.% Pd. A high fraction of the Pd unaccounted for by the perovskite is thus likely contained within both this LaPd phase as well as metallic Pd particle found throughout the phase mixture.

Several of the same oxide side phases identified by powder diffraction in the LSCrPd20 phase mixture heated in O_2 at 800 °C were observed through TEM imaging of the as-synthesized LSCrPd20 powder. Fig. 8 shows TEM images of some of these phases, including (a) bright

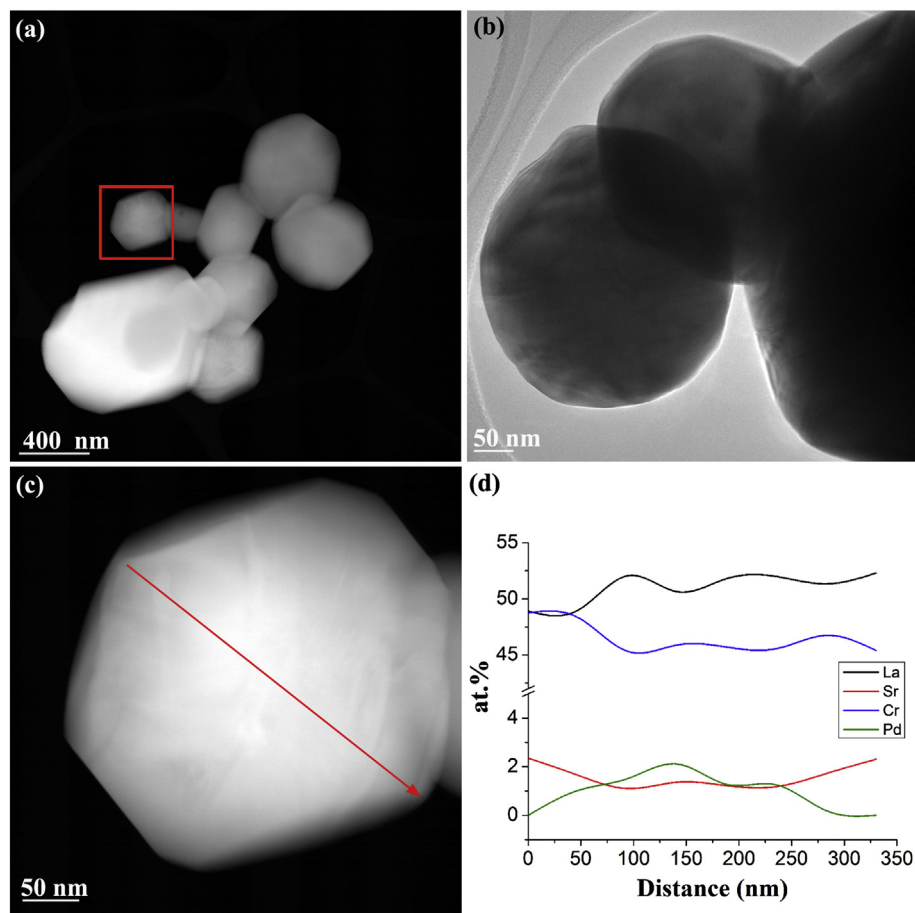


Fig. 9. Ex situ TEM imaging analysis of the LSCrPd20 perovskite after heating in $\sim 10\% \text{H}_2/3\% \text{H}_2\text{O}$ in Ar at 800 °C for 6 h showing: (a) HAADF imaging of multiple perovskite particles; (b) TEM bright field image of a perovskite particle at higher magnification; (c) HAADF imaging of a perovskite particle from "a" zoomed (original area marked with red box) in to higher magnification; and (d) results from an EDS line scan along the line in (c). (For interpretation of the references to color in this figure legend, the reader is referred to the web version of this article.)

field imaging and (b) SAED of the Pd-containing oxide La_4PdO_7 along the [154] zone axis as well as (c) higher magnification showing small Sr- and Cr-containing oxide particles on the surface of the La_4PdO_7 phase. While electron diffraction conducted during TEM analysis identified several particles as La_4PdO_7 , as observed via high resolution powder diffraction as well, EDS analysis of a large sampling of these particles yielded an average composition of 65.6 ± 2.9 at.% La, 0.2 ± 0.2 at.% Sr, 2.2 ± 2.2 at.% Cr, and 32.0 ± 2.0 at.% Pd. These EDS results led to a calculated La:Pd ratio of 2:1 rather than of 4:1 as expected. The reason behind the deviation from the stoichiometric La:Pd ratio is not entirely understood, though it is possible that the Sr and Cr impurities could have stabilized the above composition. Other Sr- and Cr-containing oxide particles with an EDS-determined average composition of 15 at.% Sr and 85 at.% Cr were also observed on the La_4PdO_7 surface and are highlighted in Fig. 8c with arrows. The Sr:Cr ratio of these oxides observed in the phase mixture ranged from 1:1 (likely SrCrO_4 , often observed via powder diffraction) to as high as 6:1 (as observed here). The small, ~50 nm diameter size of these higher Sr content oxides could also explain why they were not observed via powder diffraction, as could their possible instability at the high temperature under which diffraction measurements occurred.

The LSCrPd20 phase mixture examined by TEM in Figs. 7 and 8 was heated in ~10% H_2 /3% H_2O in Ar at 800 °C for 6 h, similar to the treatment of the LSCrPd10 powder. This reduced powder was analyzed ex situ with TEM, the images and results from which are shown in Fig. 9. Perovskite particles, which can be seen via HAADF imaging in Fig. 9a and c and via bright field TEM imaging in Fig. 9b, were the majority phase identified, consistent with diffraction measurements on

LSCrPd20 as well as TEM/STEM results on LSCrPd10 which both found the perovskite did not decompose after reduction. Multiple perovskite particles were analyzed by EDS and found to have an average composition of 51.2 at.% La, 1.9 at.% Sr, 45.6 at.% Cr, and 1.2 at.% Pd, as listed in Table 5. The Pd content within the reduced LSCrPd20 perovskite thus decreased compared to the as-synthesized perovskite sample, a strong indicator that Pd exsolution out of these perovskites is occurring to some degree. Indeed, further EDS measurements using line scan analysis (sampling line in Fig. 9c and results in Fig. 9d) found that the Pd content of the particles decreased from 2.1 at.% at the center to zero at the edges. The degree of Pd exsolution from the perovskite lattice does seem to be very low, however, as virtually no nanometer-sized Pd metal particles were observed near the perovskite particles, as shown in Fig. 9a–c. Given the high number of secondary phases observed in the LSCrPd20 phase mixture via powder diffraction and TEM, it is thus likely that most of the metallic Pd, which was observed via in situ powder diffraction in reducing conditions, originates from these minority products.

A large amount of metallic Pd, which was not found on the surfaces of the perovskite particles after reduction, was identified on the surfaces of several secondary phase particles, notably several La-rich phases. Fig. 10 shows TEM/STEM imaging analysis of metallic Pd nanoparticles on top of these La-rich surfaces via different magnifications bright field images (a-b); EDS line scan analysis (c) confirming that the support surface is La-rich while the nanoparticles are Pd-rich; and HR image (d) of the La-rich support surface for a particle ~35 nm in diameter. Fast Fourier transform structural analysis (insets in Fig. 10d) on the HR TEM images identified the particle as LaPd_2O_4 surrounded by the monoclinic B-type

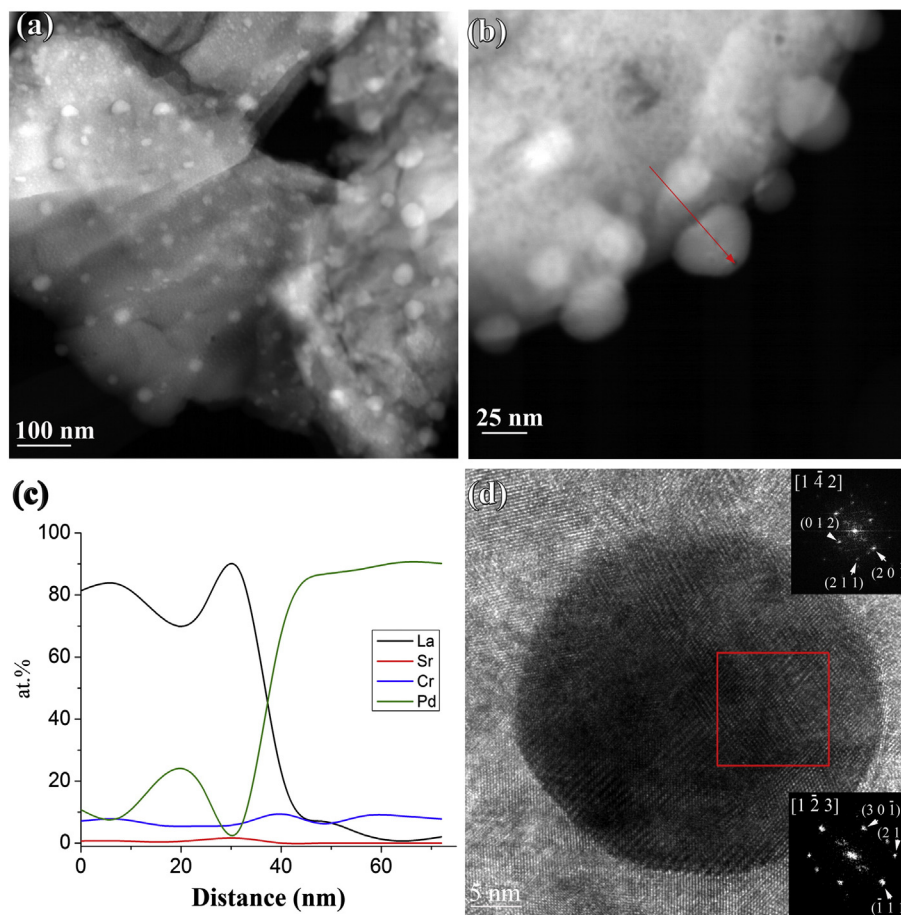


Fig. 10. Ex situ electron imaging analysis of secondary La-rich and Pd-rich phases observed in the LSCrPd20 mixture after heating in ~10% H_2 /3% H_2O in Ar at 800 °C for 6 h, including: (a), (b) HAADF images of the metallic Pd nanoparticles (bright contrast) on the surface of La_2O_3 (darker contrast); (c) results from the EDS line scan of the Pd nanoparticle and La-rich surface along the line in “b”; and (d) a HR image of the La-rich surface (bright) for a particle ~35 nm in diameter (dark), with fast Fourier transforms corresponding to LaPd_2O_4 (top, zone axis = [1 4 2]) and the monoclinic B-type La_2O_3 polymorph (bottom, zone axis = [1 2 3]) displayed as insets.

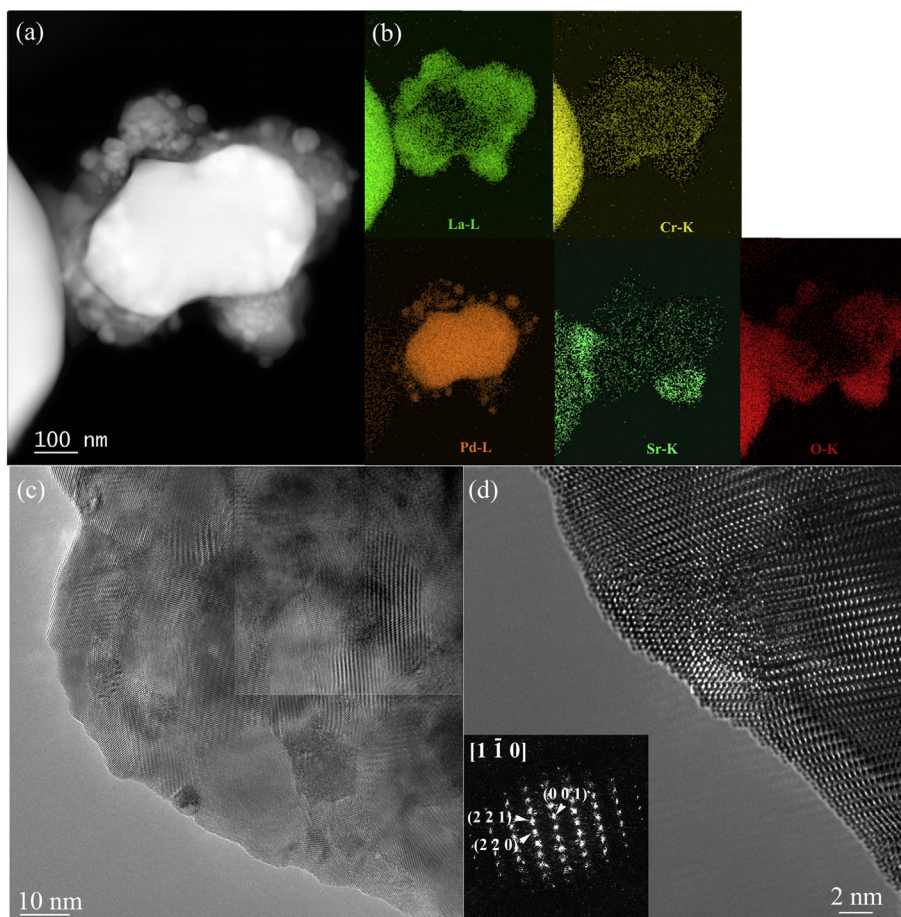


Fig. 11. Ex situ TEM/STEM analysis of La- and Pd-containing phases identified in the LSCrPd20 mixture after heating in $\sim 10\% \text{H}_2/3\% \text{H}_2\text{O}$ in Ar at 800°C for 6 h, including: (a) a HAADF image displaying typical particle morphology; (b) results from EDS elemental mapping of La, Sr, Cr, Pd, and O on the particles shown in (a); HR imaging showing (c) different grains, (d) HR image with fast Fourier transform analysis (zone axis = $[1\bar{1}0]$) identifying the particles as La_7Pd_3 in the inset.

La_2O_3 polymorph, which was further confirmed by EDS (34.6 at.% La and 65.4 at.% Pd). This is reasonable, as significant amounts of La_4PdO_7 , a phase known to decompose to PdO, metallic Pd, and La_2O_3 in reducing conditions [53,54], were observed in the LSCrPd20 mixture both as-synthesized and during heating at 800°C in O_2 via TEM (Fig. 8) and powder diffraction (Fig. 3 and Table 3), so the products of decomposition like metallic Pd and La_2O_3 should remain following exposure to H_2 . Additional

studies of Pd-containing oxides with La_4PdO_7 -like structures and different rare earth metal substituents observed nanometer-scale Pd particles on the surface of the rare earth oxide decomposition phases, as also observed here [55]. Structures of various La_2O_3 particles examined via HR TEM imaging matched those of different La_2O_3 polymorphs, including the hexagonal $P\bar{3}m1$ A-type, monoclinic $C12/m1$ B-type, and the cubic $Ia\bar{3}$ C-type [56–58]. The latter two, B- and C-type polymorphs, were present only in

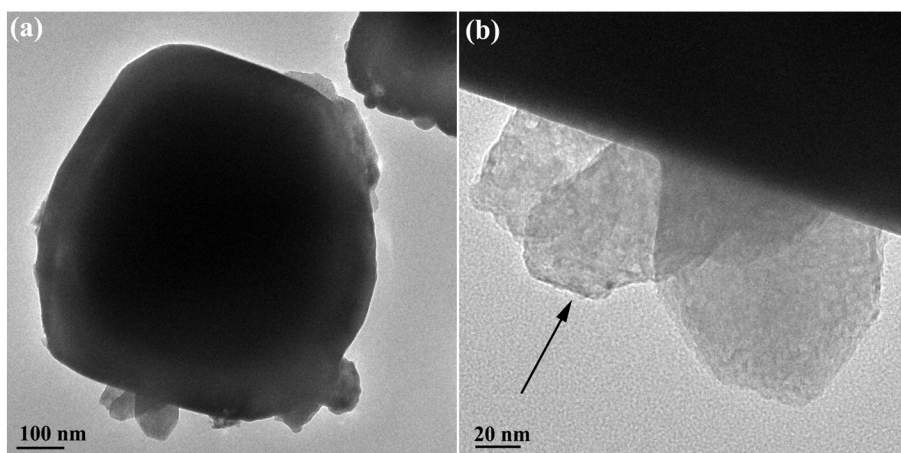


Fig. 12. (a) Lower and (b) higher magnification bright field TEM images of Sr- and Cr-containing phases identified ex situ in the LSCrPd20 mixture after heating in $\sim 10\% \text{H}_2/3\% \text{H}_2\text{O}$ in Ar at 800°C for 6 h, showing the ca. 80–100 nm sized oxide particles on the $(\text{La,Sr})(\text{Cr,Pd})\text{O}_{3-\delta}$ perovskite surface.

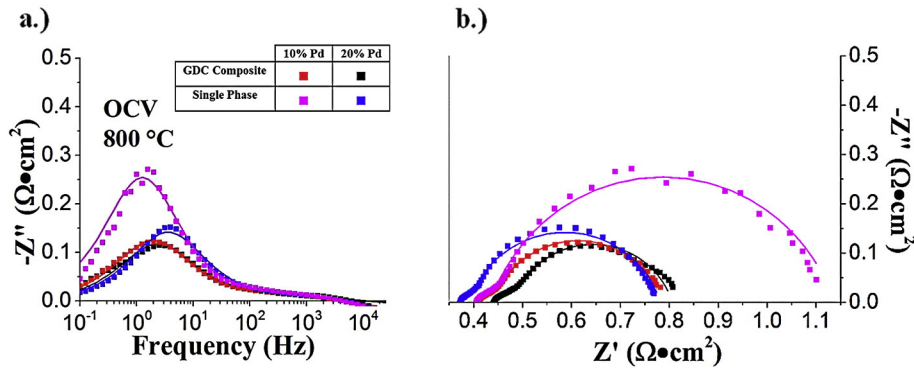


Fig. 13. (a) Bode and (b) Nyquist plots of electrochemical impedance spectra measured at OCV and at 800 °C of SOFCs with LSCrPd and LSCrPd-GDC anodes. Lines indicate fits to an equivalent circuit.

small quantities throughout the entire sample, however, as only the hexagonal A-type polymorph was observed via bulk powder diffraction. The LaPd_2O_4 phase identified, which has before been reported as structurally similar to La_4PdO_7 [59], may actually be a secondary product from the decomposition of La_4PdO_7 . While LaPd_2O_4 has rarely been observed in systems like this, it has before been synthesized via high pressure solid-state reaction of La_2O_3 and PdO in the presence of an oxidizing agent [59], so a near reverse reaction generating La_2O_3 and metallic Pd (e.g.: $2\text{LaPd}_2\text{O}_4 \rightarrow \text{La}_2\text{O}_3 + 4\text{Pd} + 2.5\text{O}_2$) under reducing conditions is possible and may be what is observed here. Since LaPd_2O_4 typically adopts a body-centered structure, the (012) and (20 $\bar{1}$) reflections observed via SAED shown in the lower inset in Fig. 10d are forbidden, indicating additional ordering as a slightly different structure, probably a superstructure.

The same Pd core/ La_7Pd_3 -shell-structured particles observed in the as-synthesized LSCrPd20 mixture were also found to be present in the H_2 reduced sample. Fig. 11 shows TEM/STEM analysis performed on some of these particles, including (a) HAADF imaging of the basic particle morphology with (b) EDS elemental mapping results showing La, Sr, Cr, Pd, and O distribution on the same particle as well as HR imaging showing (c) different grains and (d) higher magnification with fast Fourier transform analysis showing the La_7Pd_3 structure. These results clearly show that a Pd core/ La_7Pd_3 -shell structure is preserved in this ex situ reduced sample, most notably in the EDS elemental mapping in Fig. 11b which shows La distributed on the outside of the particle and Pd concentrated in the inside of the particle. EDS elemental mapping of Pd also shows a higher distribution of metallic Pd nanoparticles (ca. 40 nm in diameter) on the particle surfaces than the as-synthesized sample previously shown in Fig. 7. This indicates that the La_7Pd_3 is another significant source of the Pd metal nanoparticles observed in the LSCrPd20 specimen, on top

of which very little metallic Pd was observed (Fig. 7). Other La- and Pd-containing particles were also observed via HR imaging (Fig. 11c and d) and were confirmed to be, at least some of them, La_7Pd_3 by fast Fourier transform analysis (inset in Fig. 11d). EDS analysis further corroborated the presence of the intermetallic La_7Pd_3 , as the results did not detect any oxygen.

Nanometer-sized Sr- and Cr-containing oxides were again observed, as in the as-synthesized LSCrPd20 phase mixture (Fig. 8c as small (ca. 80–100 nm) precipitates. Fig. 12 shows bright field TEM imaging at (a) lower and (b) higher magnification, the nanoparticles on the outside of the larger perovskite particles. These oxide nanoparticles had an average composition of 5 at.% La, 72 at.% Sr, 14 at.% Cr, and 8 at.% Pd, which resulted in a Sr:Cr ratio of about 5:1, similar to the Sr- and Cr-containing oxides observed in the as-synthesized LSCrPd20 phase mixture. Because these oxides are still present even after treatment of the LSCrPd20 phase mixture in 10% H_2 at 800 °C for 6 h, it is probable that they were not observed by powder diffraction in Fig. 4 and Table 4 owing to their small size rather than their instability in high temperatures and reducing conditions.

3.3. Electrochemical testing

Fig. 13 shows (a) Bode and (b) Nyquist plots of EIS data at 800 °C as well as corresponding fits to an equivalent circuit, shown as lines, for SOFCs with LSCrPd10 and LSCrPd20 used as both single phase and GDC-composite anodes. Two responses were generally observed: a larger one at low frequencies (LF) and a smaller one at higher frequencies (HF). While the LF response varied with Pd and GDC content of the anodes, the HF response did not significantly change in intensity between SOFCs. The LF responses were thus attributed to anode-related processes

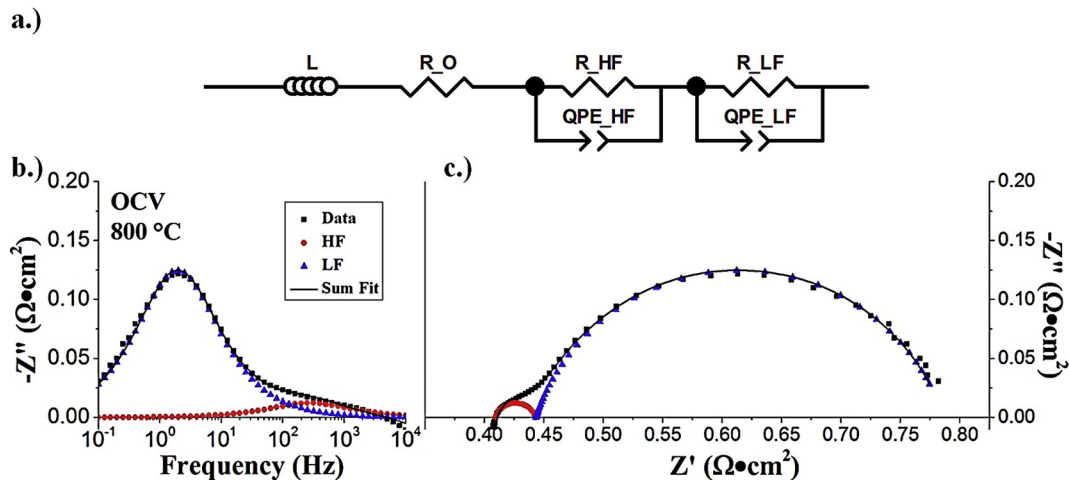


Fig. 14. (a) The equivalent circuit used for fitting data from LSCrPd anode SOFCs. (b) Bode and (c) Nyquist plots of EIS data for a representative LSCrPd10-GDC anode SOFC displaying fitting data for various equivalent circuit components.

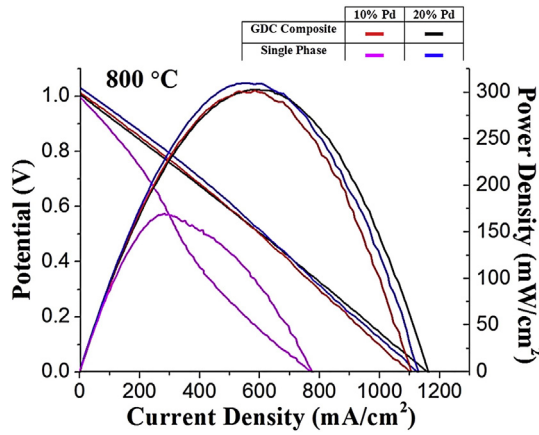


Fig. 15. Potential and power density versus current density for SOFCs with LSCrPd and LSCrPd-GDC anodes measured after 24 h of operation at 800 °C in humidified hydrogen.

which should presumably vary as anodes did from cell to cell, and the HF responses were attributed to cathode-related processes that should remain constant between cells with the same LSCF cathodes. Similar trends were reported recently to NiO-YSZ/YSZ anode and LSCF-GDC/LSCF cathode [60].

EIS data were fit to an equivalent circuit (Fig. 14a) comprising an inductor (measurement system wires), a resistor (Ohmic losses from LSGM electrolyte), and two (R-CPE) elements for the two main EIS responses observed. The exponents in the constant phase elements were held constant at $n = 0.8$ since this both provided a reasonable fit for responses at each frequency and limited the number of fitting parameters that varied [61]. Fitting of the EIS data for an LSCrPd10-GDC anode SOFC to the equivalent circuit is displayed in Fig. 14 in the form of (b) Bode and (c) Nyquist plots. The plots show the typical good quality of the total fit, as well as approximations of individual high frequency (~250 Hz) and low frequency (~2 Hz) responses.

Fig. 15 shows the current-voltage data for SOFCs with different LSCrPd and LSCrPd-GDC anodes operated in humidified hydrogen at 800 °C for 24 h. Current-voltage curves were mostly linear, with the exception of the LSCrPd10 anode SOFC, which displayed a positive curvature at high voltage but a negative curvature at lower voltage. A similar behavior was recently reported in oxide-anode SOFCs and attributed to a hydrogen adsorption limitation [62]. The highest peak power densities ranged from 0.30 to 0.31 W cm⁻², lower than values reported previously on LSCrPd-GDC anode SOFCs [30], owing to the higher Ohmic resistances observed for the SOFCs in this study. The LSCrPd20 single phase anode SOFC yielded the highest maximum power density despite its higher polarization resistance in comparison to the LSCrPd20-GDC composite anode SOFC. This was again due to the single phase anode's lower Ohmic resistance.

Table 6 presents a summary of the performance of the LSCrPd and LSCrPd-GDC anode SOFCs, including maximum power densities and anode polarization resistances $R_{p,A}$ measured at 800 °C after 24 h of operation. Values obtained for the lower frequency EIS responses, which resulted from fitting EIS data to the equivalent circuit shown in Fig. 14, were used as values for $R_{p,A}$. Anodes containing more Pd (20%) yielded lower $R_{p,A}$ values than anodes containing less Pd (10%), as

Table 6
Electrochemical performance summary for SOFCs with anodes containing different amount of Pd.

Anode material	GDC Composite		Single Phase	
	$R_{p,A}$ ($\Omega \cdot \text{cm}^2$)	Power Density (mW cm ⁻²)	$R_{p,A}$ ($\Omega \cdot \text{cm}^2$)	Power Density (mW cm ⁻²)
LSCrPd10	0.34	302	0.70	169
LSCrPd20	0.32	303	0.39	310

Table 7

Sr/La ratio ("x"), Pd/Cr ratio ("y") assuming Sr + La = 1 and Cr + Pd = 1, in La_(1-x)Sr_xCr_(1-y)Pd_yO₃, from the EDS data for the different samples annealed in O₂ or H₂.

		Average (standard deviation)
LSCrPd10_O2	x	0.039 (0.017)
	y	0.021 (0.021)
LSCrPd10_H2	x	0.084 (0.053)
	y	0.009 (0.010)
LSCrPd20_O2	x	0.031 (0.032)
	y	0.039 (0.033)
LSCrPd20_H2	x	0.036 (0.018)
	y	0.028 (0.016)

expected, since increasing concentrations of catalytic metal substituents in perovskite oxides has been well-known to decrease anode polarization resistance [28,30]. The addition of the fast ionic conductor Gd_{0.1}Ce_{0.9}O_{2- β} (GDC) also improves the performance of the cell, giving smaller impedance responses and lower $R_{p,A}$ values upon its addition. Although some LaCrO₃-based perovskites have reported increased anode polarization losses upon addition of GDC [19], the improvement observed here for LSCrPd is presumably because LSCrPd is a good electronic conductor but not a sufficiently good ionic conductor.

4. Discussion

In a prior investigation [30], it was suspected that the Pd incorporated to the perovskite structure during synthesis and precipitate onto the surface as metallic nano-particles when the anode was exposed to reducing atmospheres. Subsequent re-exposure of the reduced powder to air essentially eliminated the Pd nano-particles. As discussed in the introduction, whether this was taking place or was an oversimplification of a more complex process was not completely clear.

To determine whether Pd solubility does occur, we need to collate the information on the composition of the different phases and in particular the perovskite. The composition of the perovskite can be written as La_(1-x)Sr_xCr_(1-y)Pd_yO₃, with x and y from the EDS results (measured at room temperature (Table 7) or by Rietveld analysis of the XRD data (Table 8)).

As a cross-validation, the compositions of the different phases (excluding temporarily the Pd issue) should be consistent with other literature. According to Peck et al. [15] the solubility of Sr in La_{1-x}Sr_xCrO₃ is $x = 0.10 \pm 0.02$ at 950 °C. The x values obtained by EDS analysis, measured at room temperature, were 0.03–0.08, while those obtained from the Rietveld analysis of the XRD data, measured at 800C in O₂ or H₂ atmospheres, were 0.07–0.16. This provides credence to our results.

A second check is to analyze the effect of replacing the La³⁺ in LaCrO_{3- δ} by divalent cations, when the decrease in the positive charge will be compensated for by oxygen vacancies and by a valence change of chromium from Cr³⁺ to Cr⁴⁺. Khattak and Cox [13] reported that La_{1-x}Sr_xCrO_{3- δ} equilibrated in air at 1200–1500 °C has a composition close to stoichiometric (meaning $\delta \rightarrow 0$) while annealed in reducing

Table 8

Sr/La ("x"), Pd/Cr ("y") assuming Sr + La = 1 and Cr + Pd = 1, as well as occupancies of oxygen, obtained by Rietveld analysis of the XRD data measured at 800 °C. The isotropic thermal parameters, U_{iso} , are given as well.

	LSCrPd10 heated in O ₂	LSCrPd10 heated in H ₂	LSCrPd20 As-synthesized (heated in O ₂)	LSCrPd20 heated in H ₂
x	0.0739	0.1630	0.0712	0.1301
y	0.0251	0.0024	0.0314	0.0143
Occupancy O	0.9992	0.9798	0.9886	0.9301
U_{iso} Sr/La	0.01428	0.01682	0.01349	0.01395
U_{iso} Pd/Cr	0.00495	0.00098	0.00473	0.00480
U_{iso} O	0.00258	0.01902	0.00676	0.00464

atmosphere it deviates. Later, Mizusaki et al. [63] analyzed the nonstoichiometry of $(\text{La,Sr})\text{CrO}_{3-\delta}$ as a function of temperature and oxygen partial pressure. In the region of $\text{PO}_2 > 10^{-5}$ atm, δ was found to be close to 0. With decreasing PO_2 , δ increased and asymptotically reached $x/2$, meaning that for $\text{La}_{0.8}\text{Sr}_{0.2}\text{CrO}_{3-\delta}$, the values of δ should be between 0 and 0.1, depending on the atmosphere, also consistent with our results.

A final check is to sum the elements for each phase, based on the quantitative Rietveld analysis combined with either EDS or elemental ratios according to XRD for the perovskite composition, and comparing this to the nominal values. In order to do this we have to assume that all other phases except the perovskite, have nominal composition. However, Miyoshi [64] argue, based on lattice parameters, that there is probably a solid solution between LaCrO_4 and SrCrO_4 . Therefore the SrCrO_4 phase found in the current research could be $(\text{La,Sr})\text{CrO}_4$. Even with this caveat, the results are close to the nominal, providing further confidence that the compositions are reasonably well determined in the two tables.

With these cross-validations of the numbers, we turn to the issue of where the Pd is. The current investigation shows that most of Pd is not incorporated to the perovskite during synthesis but forms other Pd-rich phases, such as La_4PdO_7 (at LSCrPd20 specimen). The formation of the nano-sized Pd-particles on the surface of La_2O_3 in a reducing atmosphere is from decomposition of La_4PdO_7 or other Pd containing oxides. As was reported in the literature [65], the reduced materials can be quickly re-oxidized at elevated temperatures in air, whereupon the La_4PdO_7 starting material is formed after a very short time.

One additional point is that a significant fraction of the strontium is not incorporated into the perovskite phase, and there is a strong dependence of how much there is depending upon the oxygen chemical potential. This is not surprising; for instance it is now well established that for SrTiO_3 under oxidizing conditions there is segregation of SrO to the surface [66–68] and the surface is TiO_2 rich under reducing conditions as clearly observed in-situ when samples are reduced in the electron beam of a microscope [69]. This occurs because the lowest energy charge neutral defect is a SrO Shottky vacancy pair, and the oxygen vacancy concentration in the material is influenced by the oxygen chemical potential [70,71]. This has also been reported for a number of oxides and SOFC materials, see for instance references [72–79].

Similar observations have also been reported for a different Pd-substituted perovskite anode [35]. For the Pd-substituted anodes, it has been difficult to determine the actual mechanism for Pd improving the anode performance, because a number of phases were observed in the anodes, and it is only with an extended set of measurements and careful analysis of the x-ray data that one can determine to what extent Pd is actually substituted into the perovskite. This is very similar to some heterogeneous automotive emission catalysts such as the Pd doped perovskite, $\text{LaFe}_{0.57}\text{Co}_{0.38}\text{Pd}_{0.05}\text{O}_3$. It has been proposed that these materials maintain a high dispersion of precious metal nano-particles from the movement of Pd into and out of the perovskite lattice during the redox cycling commonly encountered in the engine exhaust gas [32, 80]. However, the ex-solution mechanism has been questioned in catalyst materials by new findings suggesting that only a small part of the metallic Pd near the perovskite surface in Pd-doped LaFeO_3 [81] is involved in the catalytic process and there are metal nanoparticles buried inside the oxide. Similar results have been reported for Pt in Pt-doped CaTiO_3 heterogeneous automotive emission catalysts [82]. Very recent in-situ results also support the idea of dissolution of the nanoparticle as a whole, rather than via the metal atoms in the perovskite [83]. These are all the inverse of encapsulation of nanoparticles when the combination of the oxide surface free energy and the interfacial free energy is less than that of the metal, in which case metal nanoparticles “sink” into the oxide [84,85]. This is similar to the very well established “Strong Metal Support Interactions” (SMSI) in many catalysts [86–90].

At least for our materials it does not appear that there are any discrete Pd nanoparticles buried in the oxide. Our results suggest that

these other systems may also be complex with multiple other metal containing oxides playing significant roles in addition to encapsulated nanoparticles. In terms of the SOFC performance the Pd helps as a catalyst, but one should not oversimplify what is taking place during oxidation/reduction regeneration.

5. Conclusions

Pd doped $(\text{La,Sr})\text{CrO}_3$ perovskite was investigated as anode material for solid oxide fuel cell application. Two nominal compositions (LSCrPd10 and LSCrPd20) were synthesized using the Pechini combustion method, resulting in form of powders. In-situ rapid acquisition powder diffraction experiments, while heating at 800 °C in air oxidizing atmosphere or in H_2/Ar reducing atmosphere, were performed at Argonne 17-BM synchrotron. The phase composition and structure were further examined ex-situ in transmission electron microscope.

According to the synchrotron diffraction data, the main phase was $(\text{La,Sr})(\text{Cr,Pd})\text{O}_{3-\delta}$ perovskite with some amount of Pd, PdO, SrCrO_4 and La_4PdO_7 (the last one found only in LSCrPd20 specimen). EDS analysis at transmission electron microscope, as well as Rietveld analysis of the XRD data, suggested that only portion of the Pd in the as-synthesized specimens was incorporated into the perovskite.

After reduction the perovskite's unit cell volume reduced by 0.2–0.3%, while the amount of Pd grew. Also, PdO and SrCrO_4 phases disappeared. The formation of the nano-sized Pd-particles on the surface of La_2O_3 in reduced LSCrPd20 specimen is from decomposition of La_4PdO_7 , probably contributing to the catalytic effect. The oxygen deficiency, δ in $(\text{La,Sr})(\text{Cr,Pd})\text{O}_{3-\delta}$, was found to be up to 0.03 at air atmosphere. Reduction changed that to 0.06–0.21. δ is typically larger in B-site substituted LaCrO_3 perovskites with less Cr on the B site, as was found in the current study.

Transmission electron microscopy also revealed that the perovskite was the main phase, but its crystal structure is a substructure of the known space group, probably connected to ordering. La-Pd rich phases were found; sometimes a Pd-rich core/La-Pd-rich shell structures were noticed.

SOFCs were assembled from these materials as anodes, $\text{La}_{0.9}\text{Sr}_{0.1}\text{Ga}_{0.8}\text{Mg}_{0.2}\text{O}_{3-\epsilon}$ (solid state reaction) as electrolyte supports, $\text{La}_{0.6}\text{Sr}_{0.4}\text{Co}_{0.2}\text{Fe}_{0.8}\text{O}_{3-\alpha}$ (LSCF, Praxair) mixed with GDC as cathode functional layers and thin layer of LDC ($\text{La}_{0.4}\text{Ce}_{0.6}\text{O}_2$; solid state reaction) as a barrier. The SOFCs were operated and tested at 800 °C for periods up to 24 h, the fuel was humidified hydrogen flow to the anode at rate of 50 sccm. Current-voltage and electrochemical impedance spectroscopy (EIS) were recorded. The improvement observed here for LSCrPd is presumably because LSCrPd is a good electronic conductor but not a sufficiently good enough ionic conductor.

This combined study of both the structural and electrochemical properties of the LSCrPd perovskites further clarifies the phase from which the catalytic Pd nanoparticles originate during the exsolution-dissolution process and what role the nanoparticles and their phase of origin play in SOFC anode performance. We demonstrate that while there is some amount of Pd dissolved in the perovskite matrix, this plays little to no role in the performance. Instead the Pd that is most active is initially in La_4PdO_7 or PdO phases, which decomposes under reducing conditions to form metallic Pd but under oxidizing conditions returns to La_4PdO_7 or PdO.

Supplementary data to this article can be found online at <http://dx.doi.org/10.1016/j.ssi.2016.09.006>.

Acknowledgements

The authors would like to acknowledge Gregory J. Halder from the X-ray Science Division, Advanced Photon Source at Argonne National Laboratory for his assistance on the in-situ synchrotron XRD experiments. Alan Nicholls from the Research Resources Center, University of Illinois at Chicago, is acknowledged for his assistance on JEOL JEM-

ARM200CF microscope. This work was primarily funded by the U.S. Department of Energy on grant number DE-FG02-05ER46255.

References

- [1] R.J. Kee, H.Y. Zhu, A.M. Sukesini, G.S. Jackson, *Combust. Sci. Technol.* 180 (6) (2008) 1207.
- [2] A.B. Stambouli, E. Traversa, *Renew. Sust. Energ. Rev.* 6 (5) (2002) 433.
- [3] N.Q. Minh, *J. Am. Ceram. Soc.* 76 (3) (1993) 563.
- [4] A. Atkinson, S. Barnett, R.J. Gorte, J.T.S. Irvine, A.J. McEvoy, M. Mogensen, S.C. Singhal, J. Vohs, *Nat. Mater.* 3 (1) (2004) 17.
- [5] B.C.H. Steele, I. Kelly, H. Middleton, R. Rudkin, *Solid State Ionics* 28 (1988) 1547.
- [6] D. Waldbillig, A. Wood, D.G. Ivey, *Solid State Ionics* 176 (9–10) (2005) 847.
- [7] Y. Matsuzaki, I. Yasuda, *Solid State Ionics* 132 (3–4) (2000) 261.
- [8] Q.X. Fu, F. Tietz, D. Stover, *J. Electrochem. Soc.* 153 (4) (2006) D74.
- [9] Y.H. Huang, R.I. Dass, Z.L. Xing, J.B. Goodenough, *Science* 312 (5771) (2006) 254.
- [10] P. Zhang, Y.H. Huang, J.G. Cheng, Z.Q. Mao, J.B. Goodenough, *J. Power Sources* 196 (4) (2011) 1738.
- [11] X.F. Zhu, H. Yan, Q. Zhong, X.J. Zhao, W.Y. Tan, *J. Alloys Compd.* 509 (33) (2011) 8360.
- [12] S. Cho, D.E. Fowler, E.C. Miller, J.S. Cronin, K.R. Poeppelmeier, S.A. Barnett, *Energy Environ. Sci.* 6 (6) (2013) 1850.
- [13] C.P. Khattak, D.E. Cox, *Mater. Res. Bull.* 12 (5) (1977) 463.
- [14] H. Yokokawa, N. Sakai, T. Kawada, M. Dokiya, *Solid State Ionics* 52 (1–3) (1992) 43.
- [15] D.H. Peck, M. Miller, K. Hilpert, *Solid State Ionics* 123 (1–4) (1999) 59.
- [16] I. Yasuda, M. Hishinuma, *Solid State Ionics* 80 (1–2) (1995) 141.
- [17] M.V. Patrakeev, J.A. Bahteeva, E.B. Mitberg, I.A. Leonidov, V.L. Kozhevnikov, K.R. Poeppelmeier, *J. Solid State Chem.* 172 (1) (2003) 219.
- [18] T. Nakamura, G. Petzow, L.J. Gauckler, *Mater. Res. Bull.* 14 (5) (1979) 649.
- [19] D.E. Fowler, J. Haag, C. Boland, D.M. Bierschenk, S.A. Barnett, K.R. Poeppelmeier, *Chem. Mater.* (2014) (140428025107009).
- [20] D.M. Bierschenk, J.M. Haag, K.R. Poeppelmeier, S.A. Barnett, *J. Electrochem. Soc.* 160 (2) (2012) F90.
- [21] J.M. Haag, S.A. Barnett, J.W. Richardson, K.R. Poeppelmeier, *Chem. Mater.* 22 (10) (2010) 3283.
- [22] J.M. Haag, B.D. Madsen, S.A. Barnett, K.R. Poeppelmeier, *Electrochem. Solid State* 11 (4) (2008) B51.
- [23] D. Fowler, A. Messner, E.C. Miller, B. Slone, S.A. Barnett, K. Poeppelmeier, *Chem. Mater.* 27 (10) (2015) 3683.
- [24] S. Cho, D.E. Fowler, E.C. Miller, J.S. Cronin, K.R. Poeppelmeier, S.A. Barnett, *Energy Environ. Sci.* (2013).
- [25] S.W. Tao, J.T.S. Irvine, *Nat. Mater.* 2 (5) (2003) 320.
- [26] S.W. Tao, J.T.S. Irvine, *Chem. Mater.* 16 (21) (2004) 4116.
- [27] R.T. Baker, I.S. Metcalfe, *Appl. Catal. A Gen.* 126 (2) (1995) 319.
- [28] B.D. Madsen, W. Kobsiriphat, Y. Wang, L.D. Marks, S.A. Barnett, *J. Power Sources* 166 (1) (2007) 64.
- [29] W. Kobsiriphat, B.D. Madsen, Y. Wang, M. Shah, L.D. Marks, S.A. Barnett, *J. Electrochem. Soc.* 157 (2) (2010) B279.
- [30] D.M. Bierschenk, E. Potter-Nelson, C. Hoel, Y. Liao, L. Marks, K.R. Poeppelmeier, S.A. Barnett, *J. Power Sources* 196 (6) (2011) 3089.
- [31] W. Kobsiriphat, B.D. Madsen, Y. Wang, L.D. Marks, S.A. Barnett, *Solid State Ionics* 180 (2–3) (2009) 257.
- [32] Y. Nishihata, J. Mizuki, T. Akao, H. Tanaka, M. Uenishi, M. Kimura, T. Okamoto, N. Hamada, *Nature* 418 (6894) (2002) 164.
- [33] Y. Nishihata, J. Mizuki, H. Tanaka, M. Uenishi, M. Kimura, *J. Phys. Chem. Solids* 66 (2–4) (2005) 274.
- [34] M. Uenishi, H. Tanaka, M. Taniguchi, I. Tan, Y. Nishihata, J. Mizuki, T. Kobayashi, *Catal. Commun.* 9 (2) (2008) 311.
- [35] T.H. Shin, Y. Okamoto, S. Ida, T. Ishihara, *Eur. J. Chem.* 18 (37) (2012) 11695.
- [36] M.P. Pechini, Method of preparing lead and alkaline earth titanates and niobates and coating method using the same to form a capacitor, U.S. Patent 3330697 (July 11, 1967).
- [37] L.F. da Silva, M.I.B. Bernardi, L.J.Q. Maia, G.J.M. Frigo, V.R. Mastelaro, *J. Therm. Anal. Calorim.* 97 (1) (2009) 173.
- [38] P.J. Chupas, K.W. Chapman, C. Kurtz, J.C. Hanson, P.L. Lee, C.P. Grey, *J. Appl. Crystallogr.* 41 (2008) 822.
- [39] A.P. Hammersley, S.O. Svensson, M. Hanfland, A.N. Fitch, D. Hausermann, *High Pressure Res.* 14 (4–6) (1996) 235.
- [40] H.M. Rietveld, *J. Appl. Crystallogr.* 2 (1969) 65.
- [41] A.C. Larson, R.B. Von Dreele (2004) 86–748.
- [42] P.A. Stadelmann, *Ultramicroscopy* 21 (2) (1987) 131.
- [43] J.M. Haag, D.M. Bierschenk, S.A. Barnett, K.R. Poeppelmeier, *Solid State Ionics* 212 (2012) 1.
- [44] B.D. Madsen, S.A. Barnett, *Solid State Ionics* 176 (35–36) (2005) 2545.
- [45] J.S. Ruiz, A.M. Anthony, M. Foex, C. R. Hebd. *Seances Acad. Sci.* 264 (17) (1967) 1271.
- [46] M. Mori, N.M. Sammes, *Solid State Ionics* 146 (3–4) (2002) 301.
- [47] R.K. Gupta, C.M. Whang, *Solid State Ionics* 178 (29–30) (2007) 1617.
- [48] J. Haglund, A.F. Guillermet, G. Grimvall, M. Korling, *Phys. Rev. B* 48 (16) (1993) 11685.
- [49] J. Waser, H.A. Levy, S.W. Peterson, *Acta Crystallogr.* 6 (7) (1953) 661.
- [50] H. Effenberger, F. Pertlik, *Zeitschrift Fur Kristallographie* 176 (1–2) (1986) 75.
- [51] C.W.F.T. Pistorius, M.C. Pistorius, *Z. Krist.* 117 (1962) 259.
- [52] F. Tonus, M. Bahout, P.D. Battle, T. Hansen, P.F. Henry, T. Roisnel, *J. Mater. Chem.* 20 (20) (2010) 4103.
- [53] M. Andersson, K. Jansson, M. Nygren, *Catal. Lett.* 39 (3–4) (1996) 253.
- [54] M. Andersson, J. Grins, M. Nygren, *J. Solid State Chem.* 146 (2) (1999) 428.
- [55] M. Andersson, K. Jansson, M. Nygren, *Thermochim. Acta* 318 (1–2) (1998) 83.
- [56] W.C. Koehler, E.O. Wollan, *Acta Crystallogr.* 6 (8–9) (1953) 741.
- [57] B. Wu, M. Zinkevich, F. Aldinger, D. Wen, L. Chen, *J. Solid State Chem.* 180 (11) (2007) 3280.
- [58] J. Felsche, *Naturwissenschaften* 56 (4) (1969) 212.
- [59] G. Kramer, M. Jansen, *J. Solid State Chem.* 114 (1) (1995) 206.
- [60] Z. Gao, V.Y. Zenou, D. Kennouche, L. Marks, S.A. Barnett, *J. Mater. Chem. A* 3 (18) (2015) 9955.
- [61] J.S. Cronin, K. Muangnapoh, Z. Patterson, K.J. Yakal-Kremiski, V.P. Dravid, S.A. Barnett, *J. Electrochem. Soc.* 159 (4) (2012) B385.
- [62] T. Zhu, D.E. Fowler, K.R. Poeppelmeier, M. Han, S.A. Barnett, *J. Electrochem. Soc.* 163 (2016) F952.
- [63] J. Mizusaki, S. Yamauchi, K. Fueki, A. Ishikawa, *Solid State Ionics* 12 (1984) 119.
- [64] S. Miyoshi, S. Onuma, A. Kaimai, H. Matsumoto, K. Yashiro, T. Kawada, J. Mizusaki, H. Yokokawa, *J. Solid State Chem.* 177 (11) (2004) 4112.
- [65] K.T. Jacob, K.T. Lwin, Y. Waseda, *Calphad* 26 (3) (2002) 385.
- [66] K. Szot, W. Speier, U. Breuer, R. Meyer, J. Szade, R. Waser, *Surf. Sci.* 460 (1–3) (2000) 112.
- [67] K. Szot, W. Speier, J. Herion, C. Freiburg, *Appl. Phys. A Mater. Sci. Process.* 64 (1) (1996) 55.
- [68] A. Gunhold, K. Gömann, L. Beuermann, M. Frerichs, G. Borchardt, V. Kempter, W. Maus-Friedrichs, *Surf. Sci.* 507–510 (0) (2002) 447.
- [69] Y. Lin, J. Wen, L. Hu, J.A. McCarthy, S. Wang, K.R. Poeppelmeier, L.D. Marks, *Micron* (2014).
- [70] M.J. Akhtar, Z.-U.-N. Akhtar, R.A. Jackson, C.R.A. Catlow, *J. Am. Ceram. Soc.* 78 (2) (1995) 421.
- [71] Y.S. Kim, J. Kim, S.J. Moon, W.S. Choi, Y.J. Chang, J.-G. Yoon, J. Yu, J.-S. Chung, T.W. Noh, *Appl. Phys. Lett.* 94 (20) (2009).
- [72] A.E. Becerra-Toledo, L.D. Marks, *Surf. Sci.* 604 (17–18) (2010) 1476.
- [73] Z. Cai, M. Kubicek, J. Fleig, B. Yildiz, *Chem. Mater.* 24 (6) (2012) 1116.
- [74] Y. Chen, W. Jung, Z. Cai, J.J. Kim, H.L. Tuller, B. Yildiz, *Energy Environ. Sci.* 5 (7) (2012) 7979.
- [75] E.J. Crumlin, E. Mutoro, Z. Liu, M.E. Grass, M.D. Biegalski, Y.-L. Lee, D. Morgan, H.M. Christen, H. Bluhm, Y. Shao-Horn, *Energy Environ. Sci.* 5 (3) (2012) 6081.
- [76] W. Jung, H.L. Tuller, *Energy Environ. Sci.* 5 (1) (2012) 5370.
- [77] J. Druce, H. Tellez, M. Burriel, M.D. Sharp, L.J. Fawcett, S.N. Cook, D.S. McPhail, T. Ishihara, H.H. Brongersma, J.A. Kilner, *Energy Environ. Sci.* 7 (11) (2014) 3593.
- [78] Y. Orikasa, E.J. Crumlin, S. Sako, K. Amezawa, T. Uruga, M.D. Biegalski, H.M. Christen, Y. Uchimoto, Y. Shao-Horn, *ECS Electrochem. Lett.* 3 (4) (2014) F23.
- [79] H. Wang, K.J. Yakal-Kremiski, T. Yeh, G.M. Rupp, A. Limbeck, J. Fleig, S.A. Barnett, *J. Electrochem. Soc.* 163 (6) (2016) F581.
- [80] H. Fukunaga, A. Fueoka, T. Takatsuka, K. Yamada, *J. Chem. Eng. Jpn* 42 (2009) s255 (Supplement).
- [81] M.B. Katz, G.W. Graham, Y. Duan, H. Liu, C. Adamo, D.G. Schlom, X. Pan, *J. Am. Chem. Soc.* 133 (45) (2011) 18090.
- [82] M.B. Katz, S.Y. Zhang, Y.W. Duan, H.J. Wang, M.H. Fang, K. Zhang, B.H. Li, G.W. Graham, X.Q. Pan, *J. Catal.* 293 (2012) 145.
- [83] T.S. Oh, E.K. Rahani, D. Neagu, J.T. Irvine, V.B. Shenoy, R.J. Gorte, J.M. Vohs, *J. Phys. Chem. Lett.* 6 (24) (2015) 5106.
- [84] P.M. Ajayan, L.D. Marks, *Nature* 338 (6211) (1989) 139.
- [85] L.D. Marks, P.M. Ajayan, *J. Mater. Res.* 5 (7) (1990) 1496.
- [86] S.J. Tauster, S.C. Fung, R.L. Garten, *J. Am. Chem. Soc.* 100 (1) (1978) 170.
- [87] S.J. Tauster, S.C. Fung, R.T.K. Baker, J.A. Horsley, *Science* 211 (4487) (1981) 1121.
- [88] H.R. Sadeghi, V.E. Henrich, *J. Catal.* 87 (1) (1984) 279.
- [89] R. Burch, in: Z. Paal, P.G. Menon (Eds.), *Hydrogen Effects in Catalysis*, Marcel Dekker, Inc., New York 1988, p. 347.
- [90] A. Dauscher, W. Muller, G. Maire, *Catal. Lett.* 2 (3) (1989) 139.